Remote Sensing of Environment 240 (2020) 111722

Contents lists available at ScienceDirect

Remote Sensing of Environment

journal homepage: www.elsevier.com/locate/rse

Reduction of structural impacts and distinction of photosynthetic pathways in a global estimation of GPP from space-borne solar-induced chlorophyll fluorescence

Zhaoying Zhang[a,b], Yongguang Zhang[a,b,c,*], Albert Porcar-Castell[d], Joanna Joiner[e], Luis Guanter[f], Xi Yang[g], Mirco Migliavacca[h], Weimin Ju[a,b,c], Zhigang Sun[i,j], Shiping Chen[k], David Martini[h], Qian Zhang[a,b], Zhaohui Li[a,b], James Cleverly[l], Hezhou Wang[m], Yves Goulas[n]

[a] International Institute for Earth System Sciences, Jiangsu Provincial Key Laboratory of Geographic Information Science and Technology, Nanjing University, Nanjing, China
[b] Jiangsu Provincial Key Laboratory of Geographic Information Science and Technology, Key Laboratory for Land Satellite Remote Sensing Applications of Ministry of Natural Resources, School of Geography and Ocean Science, Nanjing University, Nanjing, Jiangsu 210023, China
[c] Collaborative Innovation Center of Novel Software Technology and Industrialization, Nanjing, 210023, China
[d] Optics of Photosynthesis Laboratory, Institute for Atmospheric and Earth System Research/Forest Sciences, University of Helsinki, Helsinki, Finland
[e] National Aeronautics and Space Administration (NASA) Goddard Space Flight Center, Greenbelt, MD, USA
[f] Centro de Tecnologías Físicas, Universitat Politècnica de València, Camí de Vera s/n, 46022 València, Spain
[g] Department of Environmental Sciences, University of Virginia, Charlottesville, VA 22904, USA
[h] Max Planck Institute for Biogeochemistry, Hans-Knoell-Str. 10, 07745 Jena, Germany
[i] Key Laboratory of Ecosystem Network Observation and Modeling, Institute of Geographic Sciences and Natural Resources Research, Chinese Academy of Sciences, Beijing 100101, China
[j] College of Resources and Environment, University of Chinese Academy of Sciences, Beijing 100190, China
[k] State Key Laboratory of Vegetation and Environmental Change, Institute of Botany, Chinese Academy of Sciences, Beijing 100093, China
[l] Terrestrial Ecosystem Research Network, School of Life Sciences, University of Technology Sydney, Broadway, NSW 2007, Australia
[m] Farmland Irrigation Research Institute of Chinese Academy of Agricultural Sciences, Xinxiang, Henan, China
[n] LMD/IPSL, CNRS, ENS, PSL Research University, Ecole polytechnique, Université Paris-Saclay, UPMC Univ Paris 06, Sorbonne Universités, 91128 Palaiseau, France

ARTICLE INFO

Edited by: Jing M. Chen

Keywords:
Photosynthesis
Photosynthetic pathway
Chlorophyll fluorescence
Canopy structure
Spectral invariant theory

ABSTRACT

Quantifying global photosynthesis remains a challenge due to a lack of accurate remote sensing proxies. Solar-induced chlorophyll fluorescence (SIF) has been shown to be a good indicator of photosynthetic activity across various spatial scales. However, a global and spatially challenging estimate of terrestrial gross primary production (GPP) based on satellite SIF remains unresolved due to the confounding effects of species-specific physical and physiological traits and external factors, such as canopy structure or photosynthetic pathway (C_3 or C_4). Here we analyze an ensemble of far-red SIF data from OCO-2 satellite and ground observations at multiple sites, using the spectral invariant theory to reduce the effects of canopy structure and to retrieve a structure-corrected total canopy SIF emission (SIF_{total}). We find that the relationships between observed canopy-leaving SIF and ecosystem GPP vary significantly among biomes. In contrast, the relationships between SIF_{total} and GPP converge around two unique models, one for C_3 and one for C_4 plants. We show that the two single empirical models can be used to globally scale satellite SIF observations to terrestrial GPP. We obtain an independent estimate of global terrestrial GPP of 129.56 ± 6.54 PgC/year for the 2015–2017 period, which is consistent with the state-of-the-art data- and process-oriented models. The new GPP product shows improved sensitivity to previously undetected 'hotspots' of productivity, being able to resolve the double-peak in GPP due to rotational cropping systems. We suggest that the direct scheme to estimate GPP presented here, which is based on satellite SIF, may open up new possibilities to resolve the dynamics of global terrestrial GPP across space and time.

* Corresponding author at: Jiangsu Provincial Key Laboratory of Geographic Information Science and Technology, Key Laboratory for Land Satellite Remote Sensing Applications of Ministry of Natural Resources, School of Geography and Ocean Science, Nanjing University, Nanjing, Jiangsu 210023, China.
E-mail address: yongguang_zhang@nju.edu.cn (Y. Zhang).

https://doi.org/10.1016/j.rse.2020.111722
Received 6 December 2019; Received in revised form 7 February 2020; Accepted 12 February 2020
Available online 20 February 2020
0034-4257/

1. Introduction

Gross primary production (GPP) by terrestrial vegetation is the single largest CO_2 flux (Fu et al., 2019) and is commonly estimated by global land surface models supported by eddy covariance flux measurements (Beer et al., 2010; Sitch et al., 2015). GPP dynamics dominate inter-annual variability in net biome productivity (Jung et al., 2011) and are the main factors contributing to the uncertainties in current global vegetation models and thus carbon cycle projections (Anav et al., 2015; Lee et al., 2015; Mystakidis et al., 2016). The lack of observational constraints for GPP at regional to global scales is a critical gap in carbon cycle science, limiting our ability to monitor crucial ecosystem services and to better understand the factors that regulate terrestrial GPP and its multiple feedbacks within the Earth System (Friedlingstein et al., 2006; Arneth et al., 2010; Kulmala et al., 2014).

In the last decades, reflectance-based vegetation indices (VIs) and inversion of physical radiative transfer models have been widely used in estimating canopy structural (e.g. leaf area index) and biochemical parameters (e.g. chlorophyll content) (Haboudane et al., 2004; Gitelson et al., 2005; Gamon et al., 2019; Gitelson et al., 2019). However, estimating actual plant productivity from VIs requires auxiliary data, such as photosynthetically active radiation, which adds considerable uncertainty (Guanter et al., 2014). A promising tool to estimate large-scale GPP is solar-induced chlorophyll fluorescence (SIF), which is electromagnetic radiation in the 650–850 nm range emitted by chlorophyll-*a* molecules under illumination during the first steps of photosynthesis (Krause and Weis, 1991; Meroni et al., 2009; Pagán et al., 2019). In terrestrial plants, both photosynthetic carbon uptake and chlorophyll fluorescence emission are directly controlled by the amount and distribution of absorbed photosynthetic active radiation (APAR) within the canopy (Porcar-Castell et al., 2014; van der Tol et al., 2014; Damm et al., 2015; Yang et al., 2015; Miao et al., 2018; Yang et al., 2018a). Chlorophyll fluorescence is intrinsically linked to photochemical efficiency and can, under certain circumstances, track actual plant photochemistry (Genty et al., 1989; Porcar-Castell et al., 2014). Therefore, SIF is a possibly better probe for photosynthesis dynamics compared to other remote sensing measurements of vegetation. The direct link between photosynthesis and chlorophyll fluorescence indicates that SIF can be used as a proxy of GPP (Guanter et al., 2014; van der Tol et al., 2014; Rascher et al., 2015; Sun et al., 2017).

Recently, satellite retrievals of SIF from GOME-2, GOSAT, OCO-2 and TROPOMI (Joiner et al., 2013; Frankenberg et al., 2014; Köhler et al., 2018) have been used for estimating GPP either by constraining terrestrial biosphere or process-based models (Koffi et al., 2015; Lee et al., 2015; MacBean et al., 2018; Norton et al., 2018), or directly, exploiting the linear relationship between SIF and GPP (Guanter et al., 2014; Sun et al., 2017; Zhang et al., 2018b; Li and Xiao, 2019). The interest in a direct approach lies in its simplicity as it requires minimal amounts of ancillary data and parameterizations. However, this approach has not reached its full potential at the global scale due to the impact of numerous confounding factors, including species-specific physical and physiological traits, sun-viewing geometry, landscape heterogeneity including topography, and presence of photosynthetically inactive surfaces inside canopies (He et al., 2017; Migliavacca et al., 2017; Wood et al., 2017; Mohammed et al., 2019). All of them can contribute with spatial variation to the scaling by affecting the relationship between SIF and GPP. The extent to which we can scale SIF to global terrestrial GPP depends on the understanding of the relationships between SIF and GPP across biomes. Although two recent studies suggested a nearly universal GPP-SIF relationship across distinct vegetation types at the scale of large satellite pixels (Sun et al., 2017; Li et al., 2018b), many previous studies have showed that the relationships between ecosystem GPP and SIF are biome-dependent (Guanter et al., 2012; Damm et al., 2015; Sun et al., 2018) due to the existing discrepancies in species-specific physical and physiological traits. In addition, many other external factors, such as sun-viewing geometry (Zhang et al., 2018c), also affect SIF-GPP relationship.

Using measured and Soil-Canopy-Observation of Photosynthesis and the Energy balance (SCOPE) simulation data, Zhang et al. (2016) and Migliavacca et al. (2017) found that variations in canopy structure (e.g. leaf inclination) significantly affect the GPP-SIF relationships; plant functional traits, such as leaf chlorophyll content and the maximum rate of carboxylation (V_{cmax}), have a secondary but not negligible effect. Canopy-leaving SIF observed by satellite sensors only represents a portion of total canopy SIF emission (SIF_{total}) and the fraction of canopy-leaving SIF to SIF_{total} is mainly determined by the overall canopy architecture, resulting in varying relationships between canopy-leaving SIF and ecosystem GPP across different biomes (Sun et al., 2018). In addition, physiological differences between species could also prevent the global convergence of GPP-SIF relationships. For example, C_4 plants (covering 18% of the vegetated land surface (Still et al., 2003)) are able to sustain higher rates of photosynthesis at high light and high temperatures compared to C_3 plants (Genty et al., 1989), which could result in divergent GPP-SIF relationships between C_3 and C_4 plants (Wood et al., 2017). It is thus important to better understand how GPP-SIF relationships are affected by physical and physiological factors across different ecosystem types.

Here, we address the following scientific question on the use of SIF to estimate photosynthesis from both field and satellite SIF observations: How do the GPP-SIF relationships vary across biomes dominated by species with contrasting canopy structures and different carbon metabolic pathways? To achieve this goal, we conduct a global analysis of the effects of canopy structure (e.g. leaf inclination) and photosynthetic pathway (e.g. C_3 vs C_4 plants) on the GPP-SIF relationships by combining time series of SIF data from both in situ field measurements and OCO-2 satellite together with eddy covariance (EC) flux data from different biomes. Following a recent approach (Yang and van der Tol, 2018), we also estimate SIF_{total} at the leaf level to represent the integrated fluorescence emission of all leaves in the canopy (see Methods section), which is closely related to photosynthesis. A universal scheme for the direct and independent quantification of seasonal dynamics of terrestrial GPP based on SIF_{total} would constitute a significant step forward in the study of the global carbon cycle, its dynamics, and feedbacks within the Earth System.

2. Material and methods

2.1. Ground-based SIF and GPP measurements

Ground- and satellite-based far-red SIF (760 and 757 nm, respectively) observations will be compared with GPP across biomes in this study. SIF and flux data were measured during the growth stage at five field sites including one temperate forest (Harvard Forest from US, US-Ha1), one semiarid grassland (Majadas from Spain, ES-LM1) and three irrigated cropland sites (Avignon from France, FR-Avg, Jurong and Shangqiu from China, CN-Jrn, CN-Shq) (see Appendix Table A1).

CN-Jrn is located at the Jurong Observation Station of Nanjing University, Jiangsu Province, China. The mean annual temperature is 15.2 °C and mean annual precipitation is 1058.8 mm. In this study, summer rice was planted and measurements were conducted from August to October 2016. An automated field spectroscopy SIF system (Fluospec2) similar to that of Yang et al. (2018b) was developed for continuous measurements of canopy reflectance and SIF. The Fluospec2 system was placed at 8 m above the ground, including two spectrometers: HR2000+ (OceanOptics, Inc., Dunedin, Florida) with 400–1000 nm wavelength range at a spectral resolution of 3 nm for reflectance measurement and QEPro (OceanOptics, Inc., Dunedin, FL, USA) with 730–780 nm wavelength range at a spectral resolution of 0.1 nm for SIF measurement. The spectral fitting method (SFM) was used to extract the SIF at 760 nm, assuming linear functions of SIF and reflectance with wavelength at the spectral region of 757–767 nm.

Another Fluospec2 system was installed at 10 m above the ground in

CN-Shq, which is located at Shangqiu, Henan Province, China. The mean annual temperature is 13.9 °C and mean annual precipitation is 708 mm. In this study, corn was planted and measurements were conducted from June to October 2017. Details on the measurements of SIF at this site can be found in Li et al. (2020).

FR-Avg is planted with winter wheat at Montfavet near Avignon, France (Goulas et al., 2017). The mean annual temperature is about 14.6 °C and the annual precipitation is 676 mm. HR2000+ (full width at half-maximum (FWHM) 0.4 nm at 687 nm and 0.5 nm at 760 nm, Ocean Optics, Dudenin, FL, USA) was used in FR-Avg, and SIF at 760 nm was extracted with the Fraunhofer line discrimination (FLD). Measurements were conducted from 3 March (tillering) to 16 June (grain filling), 2010.

ES-LM1 is managed as a typical wood pasture (*Iberian Dehesa*) in Spain (Migliavacca et al., 2017). The mean annual temperature is ca. 16.7 °C and annual precipitation is ca. 650 mm. Continuous hyperspectral measurements were acquired using a fully automated Fluorescence Box (FLOX, JB Hyperspectral Devices, Düsseldorf, Germany) with a QEPro spectrometer (Ocean Optics, USA), which covers 650–800 nm spectral region with FWHM of 0.3 nm. SIF in the O_2-A absorption band (760 nm) was retrieved by SFM. The data were collected from March to June 2017, and NDVI with the threshold of 0.3 derived from QEPro measurement was used to exclude non-growing season data. Both spectral measurements and eddy covariance data used in this study were collected for the herbaceous layer, and therefore we refer to the vegetation type as GRA, although the site is classified as SAV following the IGBP classification.

US-Ha1 is a 70–100 year-old mixed temperate forest in central Massachusetts, USA. The dominant deciduous tree species includes red oak (*Quercus rubra*) and red maple (*Acer rubrum*). The mean annual temperature is ca. 7.5 °C and the annual precipitation is 1200 mm. At US-Ha1, a spectroscopy system (FluoSpec) was equipped with a hyper spectrometer placed at 5 m above canopy (Yang et al., 2015). The key component of FluoSpec is HR2000+ (OceanOptics, Inc., Dunedin, Florida) with a spectral resolution of ~0.13 nm in 680–775 nm. SIF was calculated at 760 nm with SFM that extracts SIF via the oxygen absorption method (O_2-A) (Meroni et al., 2009).

Ground continuous SIF and fluxes data are averaged over half-hour or hourly intervals. A sunshine sensor (BF5, Delta-T Devices, Cambridge, UK) is used in US-Ha1 and FR-Avg to measure diffuse (PAR_{diff}) and total PAR (PAR_{total}). The days with average $PAR_{diff}/PAR_{total} > 0.7$ are defined as extremely cloudy days and excluded for further analysis. For CN-Jrn, CN-Shq, and ES-LM1, the extremely cloudy days are excluded according to clearness index (actual shortwave radiation/top of atmosphere shortwave radiation) with a threshold of 0.3. The viewing zenith angle (VZAs) are set as zero for CN-Jrn, CN-Shq, FR-Avg, and ES-LM1 sites, and 30° for US-Ha1 site.

Thirty-six EC flux sites are chosen for comparison with satellite SIF data after visual checking homogeneity with MODIS land cover (LC) map (see Appendix Table A2) and the surrounding landscape for these sites is displayed in Fig. 1. A relatively small number of sites is used in this study (e.g., compared to the 64 sites used in a previous study (Li et al., 2018b)) because we find that some sites used in Li et al. (2018b) are heterogeneous or close to water. GPP values are determined after standard gap-filling and flux partitioning procedures (Reichstein et al., 2005). The net flux is partitioned into GPP and ecosystem respiration, which is estimated from night-time and extrapolated to daytime (Reichstein et al., 2005). It is important to note that the crop sites are divided into C_3 and C_4 crops according to farming practice; for example at a farm field (Rosemount- G21, US-Ro1), corn (C_4) and soybean (C_3) were planted in 2015 and 2016, respectively.

2.2. Far-red SIF data from OCO-2

We used the latest OCO-2 SIF Lite product (V8r), which provides three observation modes (nadir, glint and target). VZA is close to 0° for nadir mode but varies with time and space for glint and target modes (Frankenberg et al., 2014). Recent work has reported the directional anisotropy of OCO-2 SIF in target and glint modes, and that varying VZA affects the relationship between GPP and SIF (Zhang et al., 2018c). Both viewing direction and canopy structure effects on SIF can be reduced by deriving total canopy SIF emission (SIF_{total}) (Yang and van der Tol, 2018); all three modes were used in this study.

The retrieval of OCO-2 SIF, based on infilling of the Fraunhofer lines at 757 nm and 771 nm, is accomplished by using a singular vector decomposition technique (Guanter et al., 2012; Frankenberg et al., 2014). Only the SIF at 757 nm was used here after quality filtering owing to its stronger signal and better relationship with GPP than SIF at 771 nm (Li et al., 2018a). For each EC flux site, the SIF value at each overpass was determined as the mean value of all available observations located within a 30 km radius of the site location. Before averaging, land cover data provided in OCO-2 SIF product was used to remove water, snow, and urban pixels. Since US-IB1 is surrounded by urban areas, an adjacent location (−88.7°W, 41.86°N) was used for extracting OCO-2 SIF data. A preliminary comparison of OCO-2 SIF (757 nm) and in situ SIF of four field sites showed generally good consistencies in the amplitudes and seasonal variations (see Fig. S3 in this supplement).

2.3. Total canopy SIF emission (SIF_{total})

Canopy-leaving SIF observed (SIF_{obs}) by both ground and satellite sensors represents only a portion of fluorescence emission of all photosystems (SIF_{PS}) or all leaves (SIF_L) in the canopy. The scaling factor from SIF_{PS} to SIF_L for the far-red band is clearly lower than that for the red band. For example, Liu et al. (2018) reported that the ratio of SIF_{PS} to SIF_L for the far-red band (~1.5) was closer to 1 than that for the red band (~9). Therefore, it is sufficient to downscale far-red SIF_{obs} to SIF_L as a proxy of SIF_{PS}. Before interpreting the relationship between SIF_{obs} and GPP, the information about the escape probabilities of SIF from leaf to canopy level (f_{LC}) is required to reduce the viewing direction and canopy structure effects on SIF_{obs}. Recently, Yang and van der Tol (2018) have reported that f_{LC} can be derived from canopy bi-directional reflectance factor (BRF) as:

$$f_{LC} = \frac{BRF_\lambda}{i_0 \omega_\lambda} \tag{1}$$

where i_0 is canopy interception and ω_λ is leaf albedo (leaf reflectance + transmittance).

Spectral invariant theory is used as the theoretical basis of Eq. (1). This theory predicts that the radiation scattered by a canopy depends on the leaf albedo and three spectrally invariant structural parameters, including directional escape probability ($\rho(\Omega)$), recollision probability (p), and canopy interception (i_0) (Knyazikhin et al., 1998; Smolander and Stenberg, 2005). Therefore, BRF can be described by (Knyazikhin et al., 2013):

$$BRF_\lambda = \frac{\rho(\Omega) i_0 \omega_\lambda}{1 - p\omega_\lambda} \tag{2}$$

Similarly, f_{LC} can be expressed as (Yang and van der Tol, 2018):

$$f_{LC} = \sum_{i=0}^{+\infty} \rho(\Omega)(p\omega_\lambda)^i = \frac{\rho(\Omega)}{1 - p\omega_\lambda} \tag{3}$$

Combining Eqs. (2) and (3) leads to Eq. (1). However, it should be noted that the spectral invariant theory only holds for a dark soil background (Knyazikhin et al., 2013); therefore, Eq. (1) can only be applied under situations where soil background has negligible effect on BRF. The woody branches within the canopy could also affect the application of spectral invariant theory to some extent. To reduce the soil background effect on the calculation of f_{LC}, Zeng et al. (2019b) proposed to replace BRF with near-infrared reflectance of vegetation (NIR_V). NIR_V, the product of total BRF from both vegetation and soil

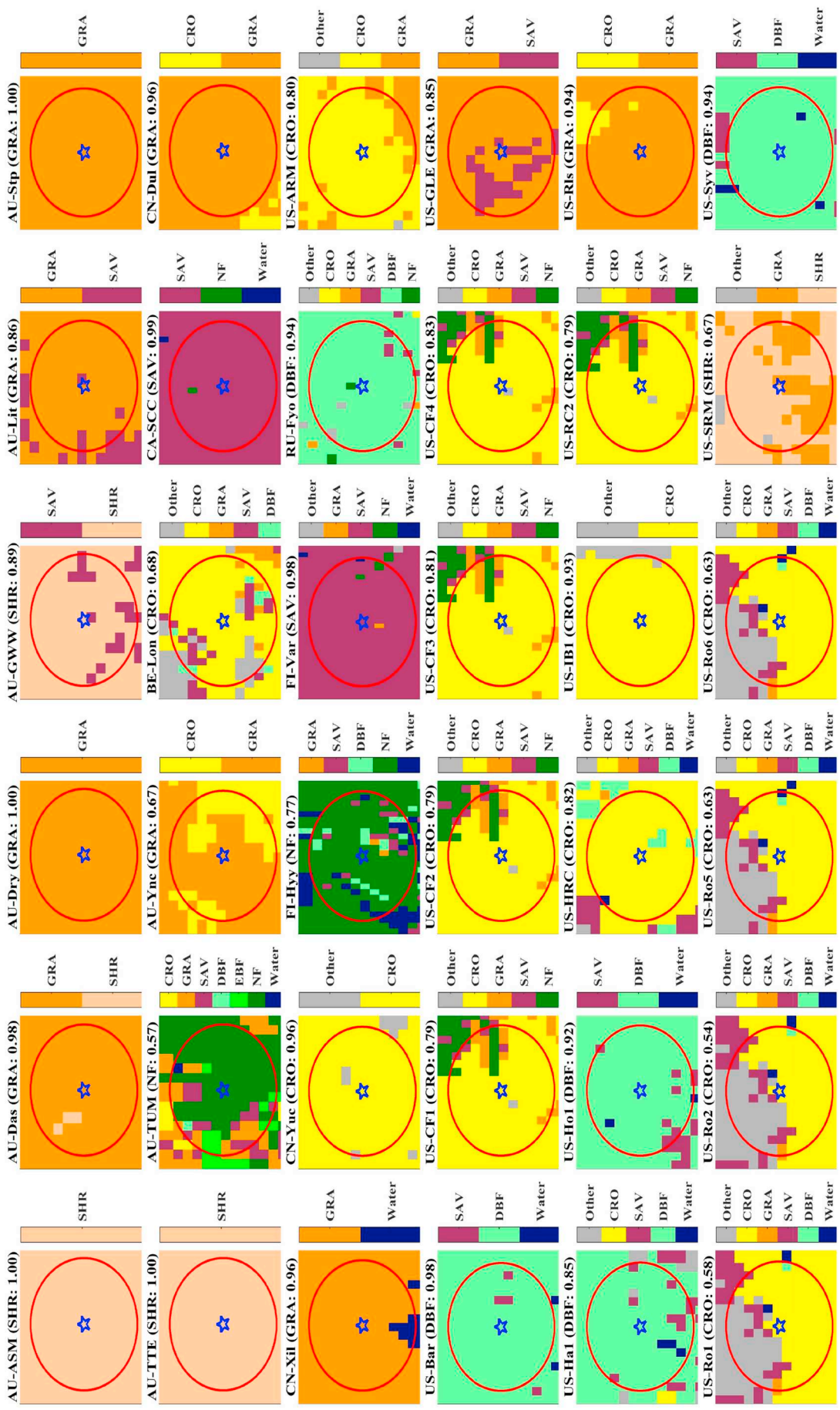

Fig. 1. Surrounding landscape at 36 flux sites (blue star). The spatial distribution of these sites is presented in Fig. S1. The base map is the land cover map based on the MODIS Land Cover Type product (MCD12C1) with the IGBP land cover classification scheme (Fig. S2). A 30 km radius around the flux tower is shown as the red circle. (For interpretation of the references to colour in this figure legend, the reader is referred to the web version of this article.)

background in a near-infrared band (NIR_T) and normalized difference vegetation index (NDVI), was originally proposed by Badgley et al. (2017) to represent the reflectance from vegetation. Therefore, Eq. (1) is rewritten as below:

$$f_{LC} = \frac{NIR_T \times NDVI}{i_0 \omega_\lambda} \quad (4)$$

In this study, NIR_T is replaced by the BRF at 760 nm for ground SIF and 757 nm for OCO-2 SIF to keep the band consistency between SIF and NIR_T. BRF is calculated as the ratio of canopy radiance to solar irradiance for both ground and satellite platforms. The BRF data for OCO-2 are calculated from the top-of-atmosphere (TOA) continuum radiances (L) as provided in OCO-2 SIF products as below:

$$BRF = \pi L/(E \times cos(\theta)), \quad (5)$$

where E is the solar irradiance at top of atmosphere at 757 nm and is set to 1259.8 W m^{-2} nm^{-1} according to the ASTM G173-03 Reference Spectra derived from SMARTS v. 2.9.2 (Gueymard, 2001), and θ is the solar zenith angle. Atmospheric correction is not conducted for OCO-2 BRF due to lack of sufficient auxiliary information. The atmospheric absorption and scattering at 757 nm is minimal on sunny days, and hence TOA BRF shows strong relationships ($R^2 = 0.999$) to top-of-canopy BRF at 757 nm (see Fig. S4 for MODTRAN simulations).

The i_0 is commonly calculated as follows (Chen and Leblanc, 2001):

where LAI and CI are leaf area index and clumping index, respectively. LAI data are obtained from MODIS C6 LAI/FPAR products (MCD15A2H) (Myneni et al., 2015). CI data provided by He et al. (2012) at a spatial resolution of 500 m are derived from the MODIS bidirectional reflectance distribution function/albedo (MCD43A1) (Schaaf et al., 2002). The Normalized Difference between Hotspot and Darkspot index (Chen et al., 2005) is used to estimate CI; more details about the CI calculation can be found in He et al. (2012). $G(\theta)$ is the mean value of geometric function and is fixed at 0.5 in this study. To match the OCO-2 footprint (1.3 × 2.25 km^2) and MODIS data with spatial resolution of 500 m, the MODIS pixels located within the boundary of OCO-2 footprint are averaged to be consistent with a single OCO-2 SIF measurement (see an example in Fig. S5 in the supplement). However, we acknowledge that the potential mismatch between OCO-2 footprint and MODIS footprints could add to the uncertainty of SIF_{total}.

To keep consistency with OCO-2 SIF_{obs}, f_{LC} (Eq. (4)) should be calculated with NIR_T and NDVI under the same sun-viewing geometry as OCO-2 SIF. NIR_T can be replaced by the BRF at 757 nm from the OCO-2 SIF product, but NDVI is not available. RossThick-LiSparseR (RTLSR) BRDF model can be used to simulate the red and near-infrared reflectance at any sun-target-viewing geometry. The parameters used to drive the RTLSR model are provided by MCD43A1 product. The simulated red and near-infrared reflectances under the same sun-viewing geometries as OCO-2 SIF are used to calculate NDVI. Since the absorption of radiation at 757 nm commonly exhibits little variation (< 0.05 for broadleaf and < 0.1 for needleleaf) (Hovi et al., 2017), the variations in ω_λ are not considered for simplicity. Further research is needed to account for this. The re-absorption effect should be taken into account when this approach is applied to red SIF (Gitelson et al., 1998; Ramos and Lagorio, 2006; Romero et al., 2018).

We define a new SIF quantity - total canopy SIF emission (SIF_{total}), which is not equal to SIF_L in magnitude, but a proxy of it:

$$SIF_{total} = SIF_{obs}/f_{LC} \propto SIF_L. \quad (7)$$

2.4. Link between SIF and GPP

Based on the light-use-efficiency concept (Monteith, 1972), the instantaneous GPP_{t0} at time t_0 can be expressed as follows (Guanter et al., 2014):

$$GPP_{t0} = PAR_{t0} \times fPAR_{t0} \times \varepsilon_{t0,p}, \quad (8)$$

where PAR_{t0} is photosynthetic active radiation arriving at the top of canopy, $fPAR_{t0}$ is the fraction of PAR absorbed by the plant canopy and $\varepsilon_{t0,\ p}$ is the overall light-use efficiency at photosystem level for the whole canopy. Instantaneous SIF_{obs} at time t_0 (SIF_{t0}) can be similarly expressed as follows:

$$SIF_{t0} = PAR_{t0} \times fPAR_{t0} \times \varepsilon_{t0,f} \times f_{PL} \times f_{LC}, \quad (9)$$

where $\varepsilon_{t0,\ f}$ is the overall light-use efficiency of fluorescence at photosystem level, and f_{PL} is the escape probability of fluorescence from the photosystem level to leaf level. Thus, a relationship between GPP_{t0} and SIF_{t0} can be established by combining Eqs. (8) and (9) as:

$$GPP_{t0} = \frac{SIF_{t0}}{f_{PL} \times f_{LC}} \times \frac{\varepsilon_{t0,p}}{\varepsilon_{t0,f}} \quad (10)$$

Compared with instantaneous GPP (GPP_i), daily mean GPP (GPP_d) conveys more accurate information on actual photosynthesis (e.g., minimizing the effect of short-term modulations due to changes in vapor pressure deficit or illumination conditions) at a temporal scale that is of interest in carbon cycle studies. In contrast to the continuous observations available from EC sites, only one snapshot per day of SIF is typically available from each satellite instrument in low Earth orbit. To obtain GPP_d, SIF_{t0} is converted to SIF_d as below (Frankenberg et al., 2011):

$$SIF_d = SIF_{t0}/\cos(\theta_{t0}) \times \int_0^{24} \cos(\theta_t)\mathrm{d}t \quad (11)$$

where θ_t and θ_{t0} are the solar zenith angles at times t and t_0, respectively. $\cos(\theta_t)$ is set as zero before sunrise and after sunset. The conversion is based on the diurnal variation of PAR and assumes constant fluorescence yield and fraction of absorbed PAR throughout the day. This day-length correction has been adopted for GOME-2, GOSAT, OCO-2 and TROPOMI SIF.

The feasibility of the day-length correction method was tested at five ground sites where continuous SIF measurements are available. SIF_i close to the overpass time (13:30) of OCO-2 SIF was converted to SIF_d using the day-length correction method for each of the five field sites. Corrected SIF_d was compared to daily averaged SIF (true SIF_d) from continuous in situ observations. We found that corrected SIF_d was well correlated with true SIF_d (slope close to 1, and $R^2 > 0.68$, Fig. 2). This indicated that the day-length correction was able to capture diurnal variations of SIF. However, it must be noted that potential deviations of

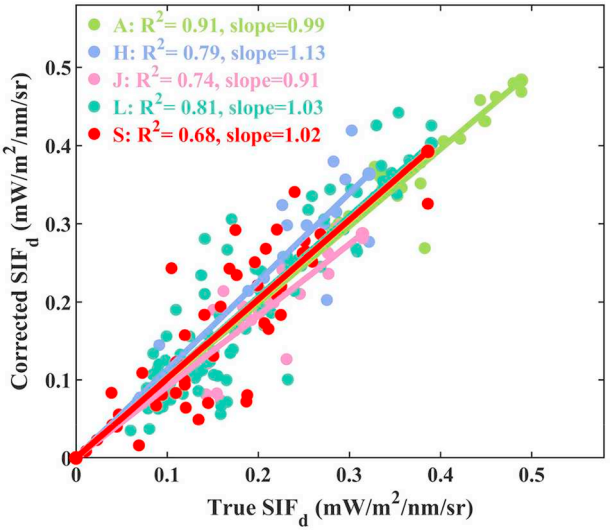

Fig. 2. Comparison of true daily SIF and corrected daily SIF from instantaneous SIF at the overpass time of OCO-2 (~13:30 h). All regressions are statistically significant ($p < 0.01$). Note: A = FR-Avg (Wheat), H = US-Ha1 (Forest), J = CN-Jrn (Rice), L = ES-LM1 (Grass), and S = CN-Shq (Corn). The cloudy days were excluded in this study when the clearness index < 0.5.

SIF from the diurnal cycle of illumination (e.g. due to photosynthetic midday depression) were not accounted for with this approach (Zhang et al., 2018a).

Similar to Eq. (10), we can link GPP_d and SIF_d using:

$$GPP_d = \frac{SIF_d}{f_{PL} \times f_{LC}} \times \frac{\varepsilon_{d,p}}{\varepsilon_{d,f}} \quad (12)$$

Eq. (12) thus represents a linear model between GPP_d and SIF_d with an intercept of zero, and hence the GPP-SIF regression models should be forced to go through the origin (Sun et al., 2017; Sun et al., 2018). However, at leaf and small canopy scales, it might be not appropriate to force SIF-GPP regression to go through the origin. Under water stress, for example, electron transport does not fully shut down and photorespiration takes the energy from the light reaction. Other metabolic pathways and routes can also kick in under certain stresses, and hence a non-zero intercept is possible. In addition, if $\varepsilon_{t0,\ p}$ and $\varepsilon_{t0,\ f}$ show non-synchronized responses to environment, SIF and GPP will exhibit a non-linear trend, and hence a non-linear model is required, such as hyperbolic model (Damm et al., 2015). It remains unclear which model is optimal at field and satellite levels, therefore, this study tested and compared three regression models (hyperbolic model, linear model with a non-zeros intercept, and linear model with a zero intercept). Generally, although nonlinear models provide a more accurate approximation to the relationship between SIF and GPP at the sub-daily or instantaneous scale (such as half-hour scale) (Damm et al., 2015; Gu et al., 2019), a linear model is frequently used to investigate the seasonal SIF-GPP relationship at the daily and longer temporal scales (Sun et al., 2017; Verma et al., 2017; Wood et al., 2017; Lu et al., 2018).

2.5. Global GPP products

In addition to EC flux tower GPP, three global GPP products are used for comparison purpose. The first one is from the FLUXCOM project (Tramontana et al., 2016), which is derived based on three machine learning methods with remote sensing data (FLUXCOM RS GPP products) or combined remote sensing and meteorological data (FLUXCOM RS + METEO GPP products) as inputs. The second one is from the Vegetation Photosynthesis Model (VPM) GPP, which is based on the light-use-efficiency concept (Zhang et al., 2017). The third one is the Boreal Ecosystem Productivity Simulator (BEPS) GPP, which is a process-based diagnostic model and separated the canopy into sunlit and shaded portions (Liu et al., 1997; Chen et al., 1999). In addition, twelve terrestrial carbon models in TRENDY project are used for comparison of GPP estimates (Sitch et al., 2015).

2.6. Land cover (LC)

The first LC data we used is from MCD12C1 V6 with a spatial resolutions of 0.05° (Friedl et al., 2010). The International Geosphere–Biosphere Programme (IGBP) classification system is employed. Except for evergreen deciduous forest (EBF) and grassland (GRA), other classes are reclassified for simplicity (following Frankenberg et al. (2011) and Sun et al. (2018)): evergreen and deciduous needleleaf forests are reclassified as needleleaf forest (NF), deciduous broadleaf forest (DBF) and mixed forest as DBF, open and close shrubland as shrubland (SHR), woody savannas and savannas (SAV) as SAV, and croplands (CRO) and cropland/natural vegetation mosaics as CRO. One hundred pixels of original MCD12C1 data are aggregated into one grid box at 0.5° resolution, and resulting grid boxes with a fraction of dominant vegetation type larger than (less than) 0.6 are assumed to be homogeneous (heterogeneous) grid boxes. These homogeneous and heterogeneous grid boxes are used for building relationships between OCO-2 SIF and FLUXCOM RS GPP for various vegetation types to show the landscape heterogeneity effect on SIF-GPP relationship. Both OCO-2 SIF observations and FLUXCOM RS GPP for 2015 are aggregated to 0.5° grid box and monthly scales. Since different biomes have unbalanced number of data points ranging from tens to thousands, the data points for each biome are binned into 20 levels. It is noteworthy that MCD12C1 data do not provide information about photosynthetic pathway, hence C_3 and C_4 crops could not be separated. In addition, crop grid boxes are commonly made up of mixed C_3 and C_4 crops, with most of them having a high fraction of C_3 crop at 0.5° resolution. Therefore, the LC of mixed crop grid boxes is assumed to be C_3 crops and will be compared with other C_3 plants. The second data source we used for LC is from Synmap Historical Landuse (Jung et al., 2011), which provides the fractions of C_4 crops and grasses as well as other C_3 plants within each 0.5° × 0.5° gridbox.

2.7. Global GPP estimation from OCO-2 SIF_{total}

The OCO-2 SIF_{total}-GPP model parameterized at 36 EC flux sites globally is used to scale OCO-2 SIF_{total} to global terrestrial GPP, and is further compared with current GPP products. Due to the discrete footprint of OCO-2 SIF and to avoid spatial gaps, all OCO-2 SIF observations for 2015–2017 are aggregated to a 1.5° spatial resolution and monthly time scale to obtain monthly averaged SIF_{total} (SIF_{month}). As indicated in the studies by Frankenberg et al. (2014) and Sun et al. (2018), the sampling bias or spatial error after the coarse aggregation and averaging is relatively small. The linear model with a zero intercept is used at the coarse spatio-temporal resolution (Sun et al., 2017; Sun et al., 2018), since most of the variations of GPP and SIF result from APAR (Li et al., 2018a; Sun et al., 2018) and GPP and SIF are zero when APAR is zero. For each gridbox, we calculate the fractions of C_3 (f3) and C_4 (f4) plants, and the monthly averaged GPP (GPP_{month}) is determined as:

$$GPP_{month} = (s3 \times f3 + s4 \times f4) \times SIF_{month} \quad (14)$$

where $s3$ and $s4$ are the slopes of linear SIF_{total}-GPP models for C_3 and C_4 plants, respectively. Eq. (14) assumes that one grid box shares the same SIF for C_3 and C_4 plants under the assumption that C_3 and C_4 plants have similar $\varepsilon_{t0,\ f}$ (Zhang et al., 2014; Wood et al., 2017). The yearly GPP (GPP_{year}) is directly averaged from GPP_{month}, and the resulting GPP_{year} uncertainty is estimated with an error propagation model (see Text S1 and Fig. S6 in the supplement). Estimated annual mean GPP from OCO-2 SIF_{total} over 2015–2017 is directly compared with other GPP products. Since FLUXCOM RS + METEO GPP does not temporally overlap with OCO-2 SIF_{total} for 2017, annual mean GPP from FLUXCOM RS + METEO GPP is derived over the most recent three years (2014–2016).

3. Results

3.1. Relationships between GPP and in-situ SIF

We firstly examine the SIF-GPP relationships for five field sites over the growing season (Fig. 3). In general, the best relationship between SIF and GPP is obtained with a hyperbolic model, followed by a linear model with a non-zero intercept (see the residual plots in Figs. S7–S9 in the supplement). For individual sites, SIF_{total} clearly improves the relationship with GPP as compared with SIF_{obs} only for the grassland site ES-LM1 (R^2 improves from 0.59 to 0.69 with a hyperbolic model); a slight improvement is obtained for the C_4 corn crop at the at CN-Shq site (R^2 from 0.85 to 0.88 for hyperbolic model). SIF_{total}-GPP relationships are degraded as compared with those of SIF_{obs}-GPP for the forest site of US-Ha1 and rice site of CN-Jrn. However, SIF_{total} significantly improves the relationships with GPP for all C_3 sites combined (R^2 increases from 0.56 to 0.72 with the hyperbolic models), with a more compact residual distribution around the zero intercept line. In addition, there is no significant difference in R^2 of SIF_{total}-GPP for the hyperbolic model (R^2 = 0.72), the linear model with a non-zero intercept (R^2 = 0.72), and the linear model with a zero intercept (R^2 = 0.71).

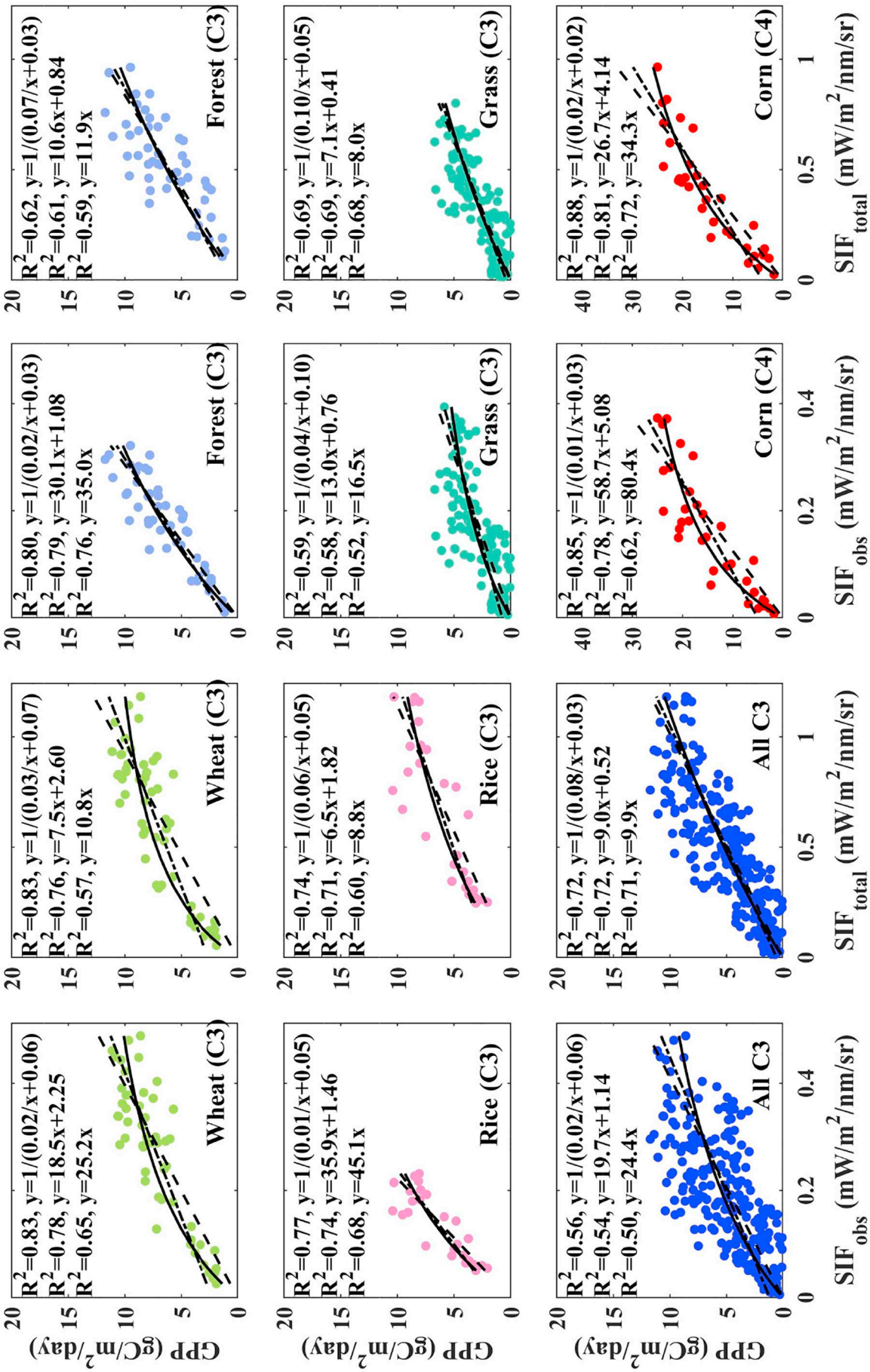

Fig. 3. Relationships between GPP and in situ SIF_{obs} and SIF_{total} for the five sites: wheat at FR-Avg, forest at US-Ha1, rice at CN-Jrn, grass at ES-LM1, and corn at CN-Shq. There is a pair of panels for each site and the set of all sites; the left panel of each pair is for SIF_{obs} and the right is for SIF_{total}. Note: C3 and C4 are C_3 and C_4 plants, respectively. Three regression methods (solid line: hyperbolic model, dash-dot line: linear model with a non-zero intercept, dashed line: linear model with a zero intercept) are used in each subplot and all regressions are statistically significant ($p < 0.01$). The standard errors of the fitted parameters are presented in Tables S2–S3 of the supplement.

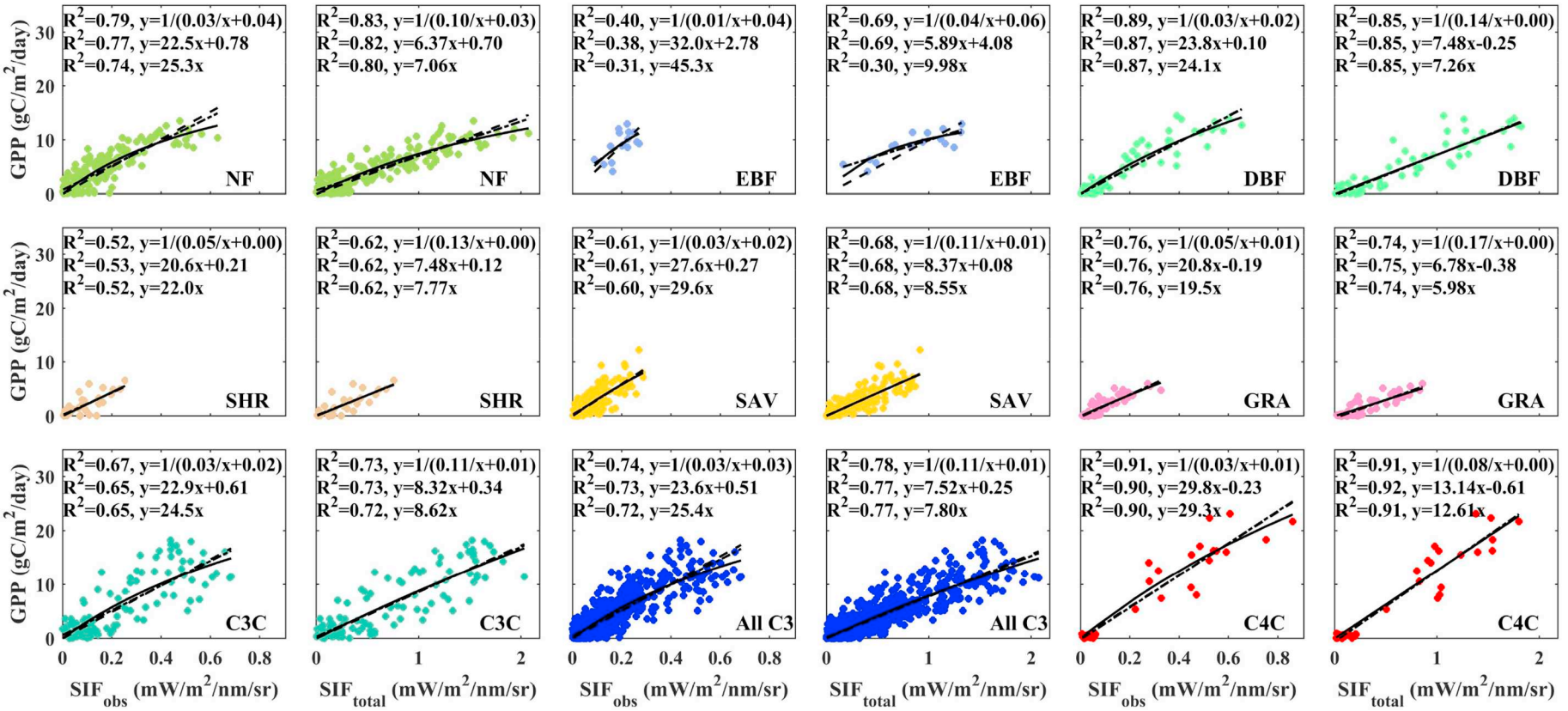

Fig. 4. Similar to Fig. 3 but uses OCO-2 SIF and is compared with GPP at more FLUXNET sites for eight vegetation types: NF (needleleaf forest), EBF (evergreen broadleaf forest), DBF (deciduous broadleaf forest), SHR (shrubland), SAV (savanna), GRA (grass), C3C (C_3 crop), and C4C (C_4 crop). There is a pair of panels for each vegetation type and the set of all vegetation types; the left panel of each pair is for SIF_{obs} and the right is for SIF_{total}. Three regression methods (solid line: hyperbolic model, dash-dot line: linear model with a non-zero intercept, dashed line: linear model with a zero intercept) are used in each subplot and all regressions are statistically significant ($p < 0.01$). The standard errors of fitting parameters are given in Tables S4–S5 of the supplement.

The larger variability and lower R^2 associated with all C_3 plants as compared with C_4 plants is attributed to the fact that four plant functional types (wheat, forest, rice, and grass) are combined as C_3 plants.

3.2. Relationships between GPP and OCO-2 SIF

Fig. 4 shows relationships between OCO-2 SIF and GPP for eight vegetation types. Unlike the results obtained at the field level, there is no clear difference in R^2 among the hyperbolic models and the linear models with either a zero or non-zero intercept for all vegetation types except evergreen broadleaf forest (EBF). Compared to the linear models, the residues of the hyperbolic models are more symmetrically distributed around zeros (see Figs. S10–S12 in the supplement). However, the linear models are sufficient for our purpose to analyze the structural and physiological effects on the SIF-GPP models at satellite level among different biomes. In addition, the 95% confidential intervals of intercepts also indicate that the assumption of a zero intercept for linear models is also valid in most cases at a coarse spatial resolution (see Table S10). When the viewing direction and canopy structure effects are reduced, SIF_{total} exhibits closer relationships to GPP for all vegetation types except DBF and GRA. Consistent with the field results, SIF_{total} significantly improves the relationships with GPP for all C_3 sites (R^2 from 0.72 to 0.77 for the linear models with zero intercept). Leave-one-out cross-validation is applied to evaluate the model accuracy for all C_3 sites and the resulting RMSE values are 1.99 to 2.08 $gC/m^2/d$ for SIF_{obs}-based models and 1.87 to 1.88 $gC/m^2/d$ for SIF_{total}-based models (Fig. S13).

The slopes of linear relationships between GPP and *in situ* SIF and OCO-2 SIF are displayed in Figs. 5 and S14. In general, the regression slopes between SIF_{obs} and GPP vary significantly among the distinct vegetation types at the field level, with a coefficient of variation (CV) of 0.43 and 0.41 for linear models with a non-zero and zero intercept, respectively (Figs. 5A and S14A). When the canopy structure effects are reduced, similar slopes among four C_3 plant sites can be observed with a CV of 0.23 and 0.19 (Figs. 5B and S14B). Although the CV of slopes of SIF_{obs}-GPP relationships at the satellite level are smaller than that at the field level (Figs. 5C and S14C), a more consistent GPP-SIF_{total} relationship is obtained for C_3 plants, with a CV of 0.13 and 0.16 for linear models with a non-zero and zero intercept, respectively (Figs. 5D and S14D).

In addition, the slope for the C_4 crop site (CN-Shq) was significantly higher than that for other C_3 sites using either SIF_{obs} or SIF_{total} for the field sites. However, this phenomenon is not observed for satellite-based SIF_{obs}-GPP relationships, in which EBF, SHR, and SAV show similar or higher slopes than the C_4 crop. On the contrary, the photosynthetic-pathway dependent GPP models clearly emerge for SIF_{total} after viewing direction and canopy structure effects on SIF_{obs} are accounted for. The steeper slope of GPP-SIF_{total} relationship for C_4 plant is due to the larger GPP of C_4 plants, while the dynamic range of SIF_{total} for C_3 and C_4 plants is shown to be the same (Fig. 4). As compared to all C_4 plants, larger fitting uncertainties are observed for C_4 crops due to the smaller number of sample points (Tables S4–S5), and hence more data should be collected for C_4 crops in the future. This result also indicates that there is an important role of photosynthetic pathway on the SIF_{total}-GPP relationships.

3.3. Relationships between FLUXCOM GPP and OCO-2 SIF

We further examine how the new GPP-SIF model (SIF_{total}) above compare to current global estimates of GPP, and analyze the relationships between FLUXCOM GPP and OCO-2 SIF_{obs} and SIF_{total} across seven vegetation types at the global scale (Fig. 6). For homogeneous grids, the slopes of SIF_{obs}-GPP relationships vary significantly among biomes with a CV of 0.24; there are smaller slopes for crop and grass and a higher slope for NF (Fig. 6A). This biome-specific slope of SIF_{obs} with respect to FLUXCOM GPP is consistent with previous work (Guanter et al., 2012; Zhang et al., 2016; Sun et al., 2018). Consistent with ground and satellite results (Figs. 3–5), the CV of the regression

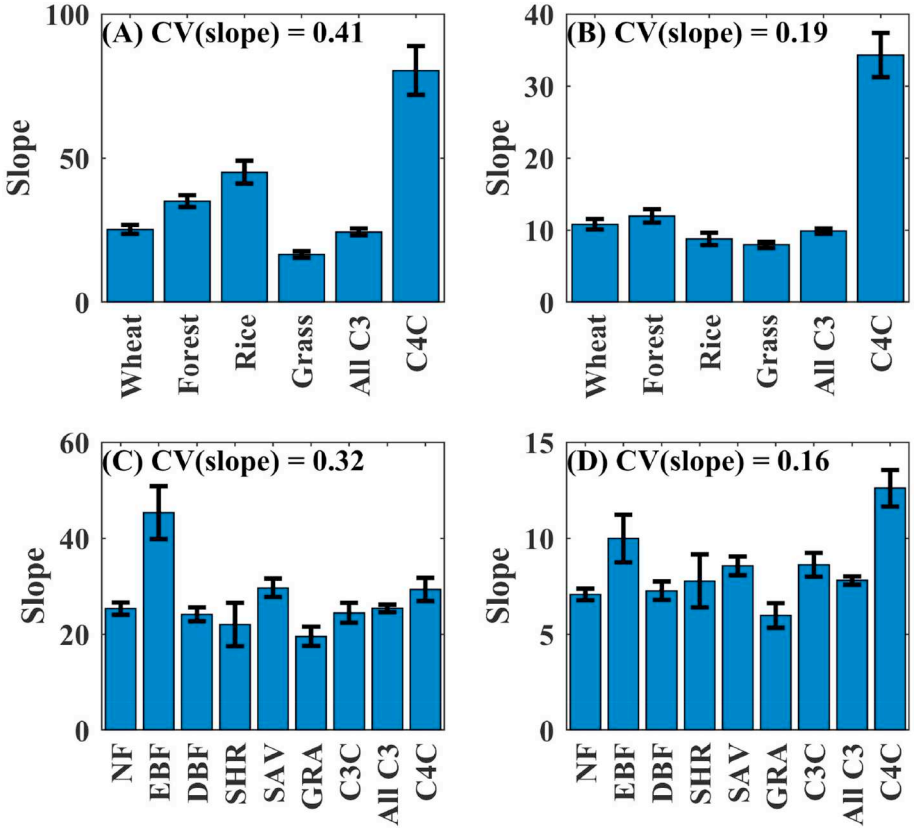

Fig. 5. Slopes of relationships between GPP and (first row) ground-based SIF and (second row) OCO-2 SIF. First column: GPP = slope × SIF_{obs}; second column: GPP = slope × SIF_{total}. CV indicates the coefficient of variation of slopes among all C_3 plants. The significance (*p*-value) of the difference in the slopes between any two biomes are presented in Tables S6–S9 of the supplement.

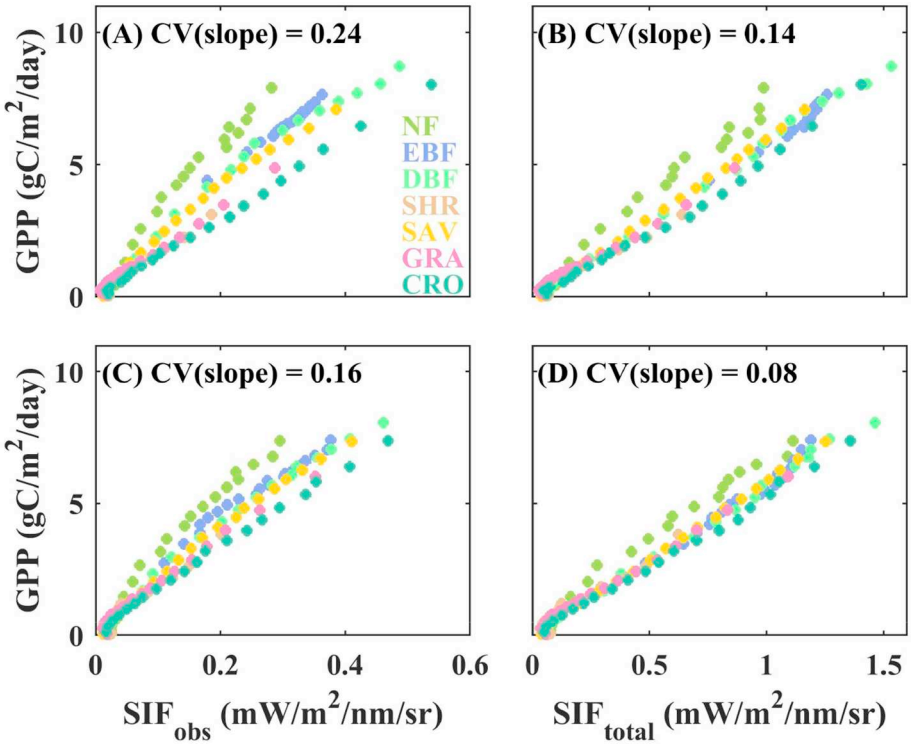

Fig. 6. Scatter plots of FLUXCOM GPP with OCO-2 (**A**) SIF_{obs} and (**B**) SIF_{total} for homogeneous 0.5° grids with dominant land cover fraction > 0.6. (**C–D**) similar to (**A–B**) but for heterogeneous 0.5° grids with dominant land cover fraction < 0.6. CV indicates the coefficient of variation of slopes among all vegetation types.

slopes of SIF_{total}-FLUXCOM GPP relationships is reduced from 0.24 to 0.14 after removing the effect of canopy structure (Fig. 6B). For heterogeneous grids, the CV of regression slopes is further reduced from 0.24 to 0.16 for SIF_{obs} (Fig. 6C) and from 0.14 to 0.08 for SIF_{total} (Fig. 6D), which is expected since biome-specific slopes are averaged and smoothed.

3.4. Estimation of global terrestrial GPP with the SIF_{total}-based model

To directly investigate the performance of the SIF_{total}-GPP relationships, we estimate annual global GPP of terrestrial vegetation with the derived SIF_{total}-based linear models with a zero intercept in Fig. 4 that are calibrated with 36 EC flux tower GPP and the corresponding OCO-2 SIF_{total}. Due to the significant difference in slopes observed between C_3 and C_4 plants, it is logical to apply two separate SIF_{total}-based GPP models for C_3 and C_4 plants. The global GPP estimates from satellite-based SIF_{total} data (Fig. 7A) are compared to current state-of-the-art GPP estimates (Fig. 7B–D). We also compare the zonally averaged and biome-averaged GPP from four different GPP estimates. The GPP estimated with OCO-2 SIF_{total} is generally consistent with FLUXCOM RS + METEO GPP and VPM GPP (Fig. 7E–F).The SIF_{total}-based GPP estimations are able to depict the spatial patterns of vegetation GPP globally, consistent with existing global GPP estimates. This agreement is also supported by the strong linear correlations between OCO-2 SIF_{total}-based GPP estimates and FLUXCOM RS + METEO and VPM GPP on a per pixel basis ($r > 0.9$, Fig. 8). Total global annual mean GPP is estimated to be 129.56 ± 6.54 PgC/year from OCO-2 SIF_{total} over 2015–2017, which is consistent with the reported values of global GPP: 102–135 PgC/year (Beer et al., 2010), 112–169 PgC/year (Anav et al., 2015), and those (113–183 PgC/year) from twelve terrestrial carbon models in TRENDY project (S3 scenario) over 2014–2016 (Fig. S15).

Continuing the spatial comparison of SIF_{total}-based GPP to the FLUXCOM RS + METEO GPP, our estimates capture the high photosynthesis of agricultural regions, such as Western Europe (Fig. S16A). Specifically, SIF-based GPP estimates capture the 'hotspots' of high photosynthesis in the US Corn Belt for the period of June to September (Fig. 9A), which are missing in the FLUXCOM GPP. This suggests underestimation of C_4 crop GPP by some current models, supporting previous findings (Guanter et al., 2014). In addition, VPM GPP also shows lower GPP than SIF_{total}-based GPP over the Amazon tropical rainforest region (Fig. 9B), which is attributed to the underestimation of VPM GPP at this region (Zhang et al., 2017).

The seasonal cycles of GPP over six selected regions (depicted in Fig. 7A) are presented in Fig. 10, which provides additional insight into the comparison of GPP estimates. For the North American crop regions, VPM and SIF_{total}-based GPP exhibits higher estimates than FLUXCOM RS + METEO and BEPS GPP during the peak of the growing seasons (Fig. 10A). BEPS GPP shows clearly higher magnitudes than other GPP estimates over Europe (Fig. 10B). Over the Asian crop regions, both VPM and SIF_{total}-based GPP are able to capture the double peak pattern of GPP caused by the double cropping system (Fig. 10C); this provides more accurate predictions of agricultural productivity and crop yields. In the Amazon rainforest and Australian shrubland, all GPP estimates exhibit a low seasonal variation (Fig. 10D and F). In the African savannas, four GPP estimates show consistently opposite seasonality of vegetation with minimal GPP in July and August (Fig. 10E).

4. Discussion

4.1. Effects of canopy structure on the GPP-SIF relationship

Accurate and direct quantification of photosynthesis at the ecosystem, landscape, regional, and global scales plays a critical role in understanding the influence of terrestrial ecosystems on the carbon cycle (Friedlingstein et al., 2014; Anav et al., 2015), the feedbacks between biosphere and atmosphere (Kulmala et al., 2004; Arneth et al., 2010), and the assessment of future climate predictions (Friedlingstein et al., 2014). Although SIF has been shown to be a promising tool to estimate GPP across various spatial scales, the use of satellite SIF

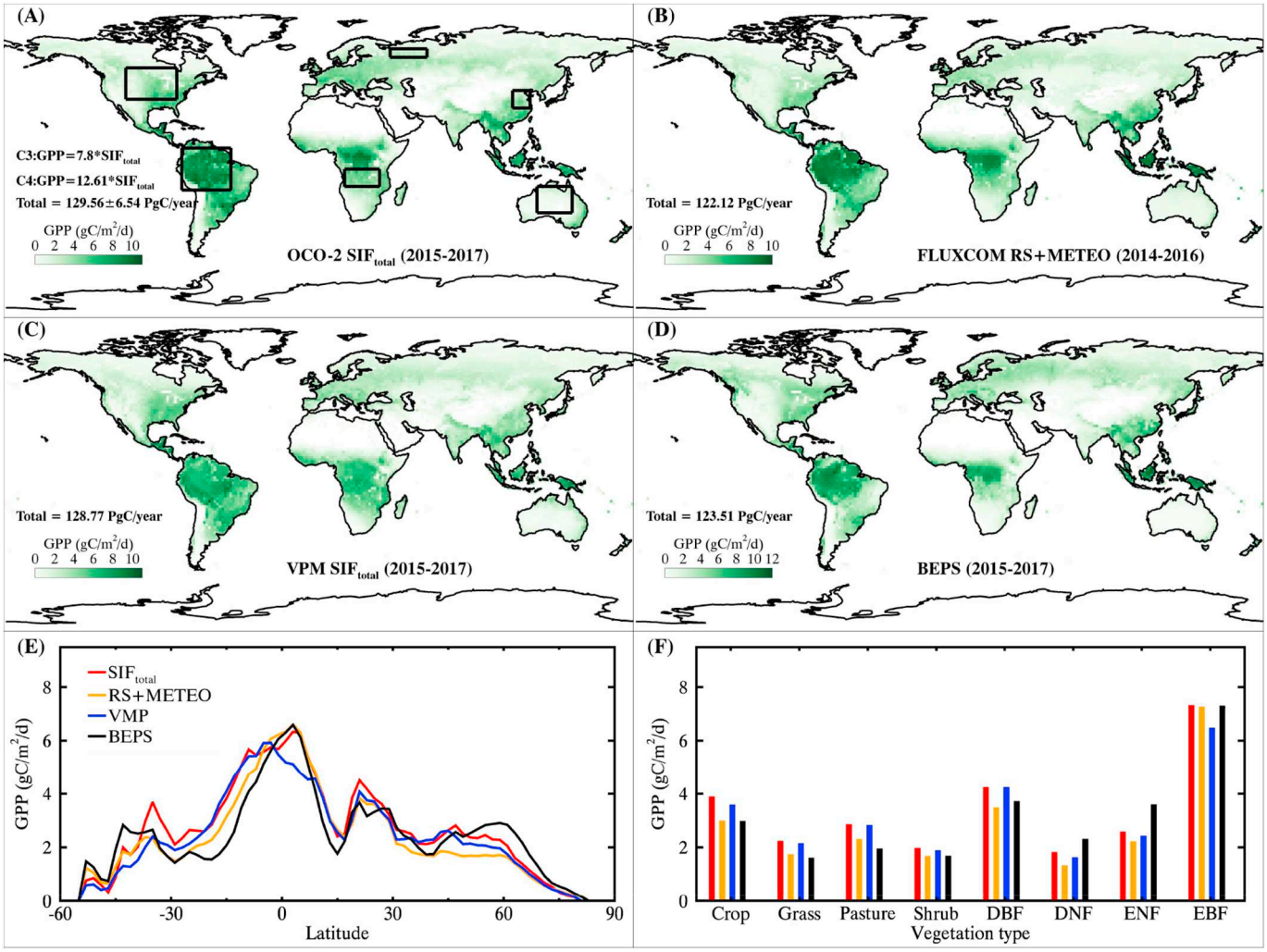

Fig. 7. Global three-year averaged GPP distribution from (**A**) OCO-2 SIF_{total}-derived GPP over 2015–2017, (**B**) FLUXCOM RS + METEO GPP over 2014–2016, (**C**) VPM GPP over 2015–2017, and (**D**) BEPS GPP over 2015–2017, and the comparison of (**E**) zonally averaged and (**F**) biome-averaged GPP. Six boxes in panel (**A**) indicate regions of interest that are further explored in Fig. 10.

observations for constraining global terrestrial GPP is hindered by the recent debate on whether the GPP-SIF relationship is biome-specific (Frankenberg et al., 2011; Guanter et al., 2012; Zhang et al., 2016) or consistent across biomes (Sun et al., 2017; Li et al., 2018b). Here, we present an ensemble analysis of GPP-SIF relationships combining satellite and ground-based SIF observations with flux tower GPP across distinct biomes. Statistically significant but biome-specific GPP-SIF relationships are obtained after time of day adjustment (Figs. 3–5). This result agrees with many previous studies but does not support the slope convergence recently observed by Sun et al. (2017) where data from three contrasting flux sites were used. This discrepancy may be due to differences in number of sites or temporal coverage between studies. In

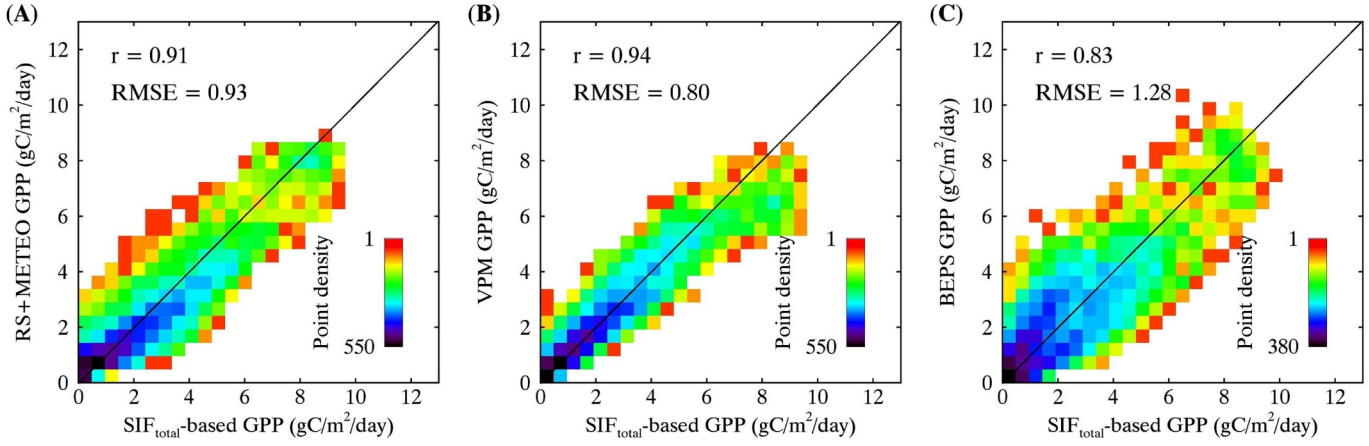

Fig. 8. The relationships between OCO-2 SIF_{total}-based GPP and (**A**) FLUXCOM RS + METEO GPP, (**B**) VPM GPP, and (**C**) BEPS GPP.

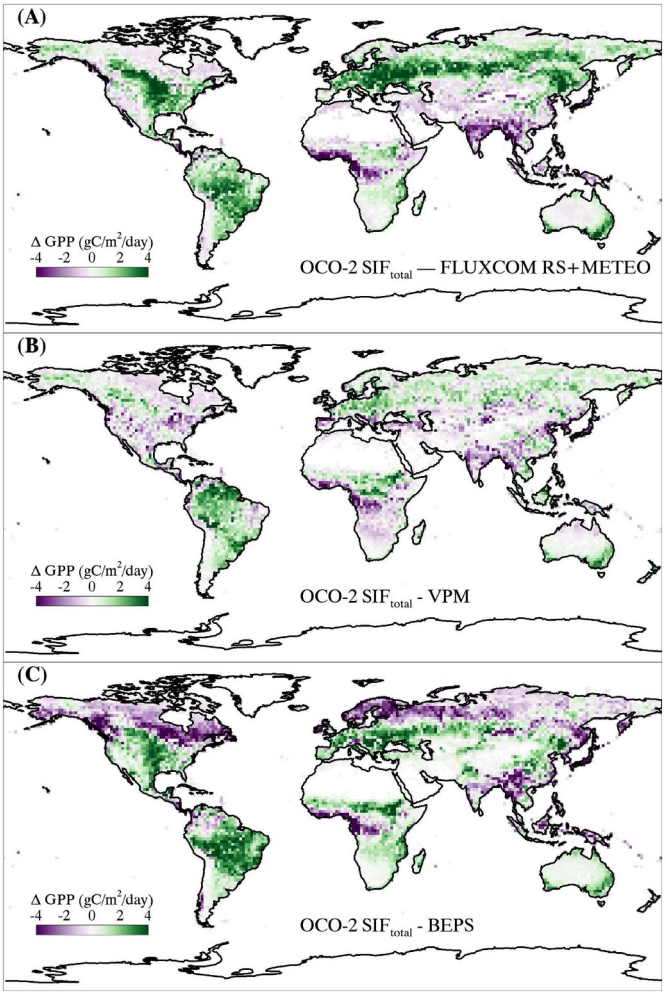

Fig. 9. Spatial distribution of mean GPP difference between SIF_{total}-derived GPP (2015–2017) and (**A**) FLUXCOM RS + METEO GPP (2014–2016), (**B**) VPM GPP (2015–2017), (**C**) BEPS GPP (2015–2017) averaged over June–September.

addition, Li et al. (2018b) suggested a nearly universal linear relationship between OCO-2 SIF and GPP across biomes, which may be biased by the landscape heterogeneity (Fig. 6). Although the CV at the satellite level is smaller than that at the field level, there are 14 pairs of biomes (only C_3 plants) showing significantly different ($p < 0.05$ in Table S9) slopes of GPP-SIF_{obs} relationships for the linear model with a zero intercept.

Compared with observed canopy-leaving SIF_{obs} from remote sensing measurements, the slope of the relationship between GPP and SIF_{total} exhibits less variability. The smaller CV in slopes of SIF_{total}-GPP relationships across biomes for C_3 plants suggests a possibility to establish a more consistent GPP model from SIF_{total} globally. Our results suggest that SIF_{total} can be used as a proxy of canopy photosynthesis regardless of different canopy architectures across biomes for C_3 plants. After reducing canopy architecture effects from the observed SIF, the SIF_{total} signal is closer to the leaf level SIF signal and therefore should be better connected to the dynamics of photosynthesis (Liu et al., 2018; Yang and van der Tol, 2018; Zeng et al., 2019a; Zhang et al., 2019). This result also indicates that the effects of canopy structure can be mitigated using BRF from reflectance measurements under actual scenarios. With the gradually increasing spatial and temporal coverage of satellite SIF products, e.g. the future Fluorescence Explorer (FLEX) mission by the European Space Agency that should deliver bi-weekly SIF data at approximately 300 m spatial resolution (Drusch et al., 2017), the SIF_{total}-based approach will open up a new range of possibilities for mapping terrestrial GPP (Zhang et al., 2019).

4.2. Effect of photosynthetic pathway on the GPP-SIF relationship

The emerging photosynthetic-pathway dependent GPP-SIF relationships suggest that different plant growth strategies should be considered. In this study, we examine the dominant role of canopy structure on GPP-SIF relationship that controls the escape probability f_{LC} (Migliavacca et al., 2017). However, the more consistent $\varepsilon_{t0,\,p}/\varepsilon_{t0,\,f}$ ratio found in C_3 plants may not hold for C_4 plants. This could be the result of photorespiration that decreases the overall efficiency of photosynthesis in plants with C_3 metabolism but has little effect on C_4 plants (Pearcy and Ehleringer, 1984; Collatz et al., 1992). Therefore, C_3 plants tend to exhibit smaller photosynthetic efficiency, or $\varepsilon_{t0,\,p}$ than C_4 plants (Ehleringer and Björkman, 1977; Pearcy and Ehleringer, 1984;

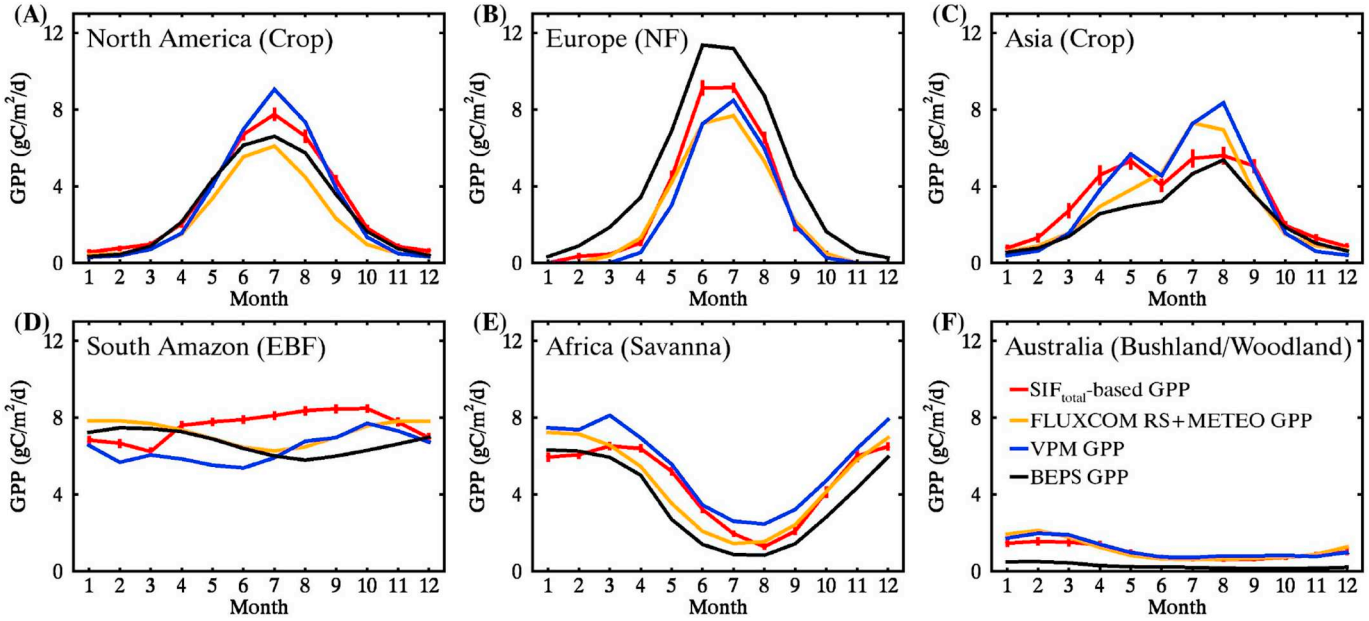

Fig. 10. Seasonal dynamics of four GPP estimates over (**A**) North America (crop), (**B**) Europe (needleleaf forest, NF), (**C**) Asia (crop), (**D**) South America (evergreen broadleaf forest, EBF), (**E**) Africa (savanna), (**F**) Australia (bushland/woodland). The standard error is shown only for SIF_{total}-based GPP for simplicity.

Beadle and Long, 1985; Krall and Edwards, 1992; Kellogg, 2013; Zhang et al., 2014; Gitelson et al., 2018), supporting the smaller slope in SIF-GPP relationships found for C_3 plants as compared with C_4 plants (Figs. 3–5).

However, similar canopy-level SIF values are produced for both crop types (i.e., similar $\varepsilon_{t0,\ f}$) if everything else is kept equal based on SCOPE simulations (Zhang et al., 2014). This is supported by the same dynamic range of OCO-2 SIF_{total} for C_3 and C_4 plants (Fig. 4). Due to the higher CO_2 assimilation rate of C_4 plants (Pearcy and Ehleringer, 1984; Collatz et al., 1992), the higher $\varepsilon_{t0,\ p}/\varepsilon_{t0,\ f}$ will produce a higher GPP-SIF slope than that for C_3 plants (Figs. 3–5). After accounting for canopy structure effects, the statistically significant ($p < 0.01$ in Table S9) difference in slopes of OCO-2 SIF-GPP relationships for C_3 and C_4 plants may be attributed to the different $\varepsilon_{t0,\ p}$ under similar $\varepsilon_{t0,\ f}$. The slope for C_4 plants is 1.62 times higher than that for C_3 plants (Fig. 4), and the ratio agrees well with that (1.5) assumed in the study of Zhang et al. (2017). This difference of slope may not be only due to the photorespiration of C_3 and C_4 plants. Other environmental factors, such as temperature, water supply and CO_2 concentration, may also need to be accounted for (Ehleringer and Björkman, 1977; Sage and Kubien, 2007; Ghannoum, 2008). Due to the statistically significant ($p < 0.01$ in Table S9) difference in the slopes for C_3 and C_4 plants, therefore, it is necessary to establish SIF_{total}-based GPP models for C_3 and C_4 plants separately (Fig. 4). Considering the dominance of C_3 plants globally, however, a consistent GPP model from SIF_{total} across different C_3 vegetation types observed here would help improve regional and global GPP estimates based on remotely sensed SIF observations.

If we do not consider C_4 plants and use the SIF_{total}-GPP model of C_3 plants alone for all plants, the global GPP is predicted as 126.82 PgC/year. As expected, ignoring the difference of C_3/C_4 plants would underestimate the GPP from C_4 crops by 2.74 PgC/year, which accounts for about 15% of GPP from crops. The OCO-2 observations are aggregated into 1.5° grid boxes in our study and many grid boxes contain a mixture of C_3 and C_4 plants. We assume that a linear relationship between SIF and GPP holds for mixed soybean (C_3) and corn (C_4) pixels (Wood et al., 2017). Using the fractions of C_3 and C_4 plants would lead to accurate GPP estimates for individual grid boxes. This separate consideration for C_3 and C_4 plants and using the fraction of C_3 and C_4 plants are also adopted in the vegetation photosynthesis model (VPM) to map global GPP production with 500 m spatial resolution (Zhang et al., 2017). Recently, Li and Xiao (2019) have reported the estimated global terrestrial GPP of 135.5 ± 8.8 PgC/year from artificial SIF, which is derived from MODIS EVI, air temperature, photosynthetically active radiation, and vapor pressure deficit. In addition, the separation of C_3 and C_4 plant is not considered in their study. Our results highlight the need for separate models for C_3 and C_4 plants as well as an updated fractional map for C_3/C_4 plants.

4.3. Scaling SIF_{total} to terrestrial GPP globally

Interestingly, the emerging photosynthetic-pathway dependent GPP-SIF relationships for C_3 and C_4 plants provide very simple models for estimating GPP. Due to its physiological link to photosynthesis and absorbed PAR, SIF has been recently shown to provide a constraint on GPP globally (Lee et al., 2015; Norton et al., 2018). However, the parameterization of SIF-based models is still a critical issue due to inconsistency of GPP-SIF relationships among distinct biomes. An important implication of our work is that the dependence of GPP-SIF_{total} relationships on land cover data can be relaxed and only a fractional map of C_3/C_4 plants is needed to estimate GPP globally. Despite the use of only two separate models for C_3 and C_4 plants, our estimates of global GPP agree well with the independent FLUXCOM RS + METEO and VPM products both in the spatial patterns and magnitude of GPP at the global scale. It is not surprising that our GPP estimates are able to capture the spatial patterns of vegetation productivity over the globe since OCO-2 SIF provides a reasonable depiction of the spatial patterns of vegetation (Norton et al., 2018; Sun et al., 2018).

Our data-driven SIF_{total}-based model provides a novel and straightforward approach for estimating terrestrial GPP by considering and correcting for the effect of canopy structure and the C_3/C_4 photosynthetic pathway. We demonstrate the potential of SIF_{total} as a direct proxy of terrestrial GPP at the global scale, bypassing the need to use complex models and biome-specific parameterizations to assimilate the information. In addition, the SIF_{total}-based GPP estimates can be applied to the study of feedbacks related to anthropogenic activities (Zhu et al., 2016) or CO_2 fertilization (Smith et al., 2016) on the terrestrial vegetation. Although it is not possible to fully validate our annual mean GPP estimate, our estimates in the magnitude are in line with previous studies (Beer et al., 2010; Anav et al., 2015; Campbell et al., 2017; Joiner et al., 2018) and this good agreement supports the usefulness of a consistent SIF-based GPP model after mitigating canopy structure effects. However, it should be noted that our aim is not to provide a definitive estimate of global annual GPP from SIF; rather, we intend to investigate whether simple and consistent SIF-based GPP models can be obtained.

5. Conclusion

Our results show that the slopes of observed canopy-level SIF with respect to GPP are significantly different among biomes; this is mainly due to canopy structure effects. After accounting for these effects using BRF from corresponding reflectance measurements, a more consistent GPP-SIF relationship can be derived across biomes for C_3 plants as shown with both ground- and satellite-based SIF observations. On the other hand, a separate GPP-SIF relationship still exists for C_3 and C_4 plants which is attributed to variations of photosynthetic pathway. Our work demonstrates the potential to establish photosynthetic-pathway dependent models to estimate GPP from SIF after accounting for the canopy structure effects. Based on our OCO-2 SIF_{total}-based GPP model for C_3 and C_4 plants, we obtain an estimate of global annual GPP of 129.56 ± 6.54 PgC/year. This is in line with estimates from a state-of-the-art up-scaled flux tower product and a vegetation photosynthesis model in terms of both magnitude and spatial patterns. This provides confidence that the SIF_{total}-based model produces robust estimates of global terrestrial vegetation photosynthesis. The photosynthetic-pathway dependent SIF_{total}-based model for estimating GPP proposed in this study provides other ways of using SIF to resolve the dynamics of global terrestrial GPP across space and time.

CRediT authorship contribution statement

Zhaoying Zhang:Conceptualization, Methodology, Software, Formal analysis, Writing - original draft, Writing - review & editing.**Yongguang Zhang**:Conceptualization, Formal analysis, Writing - original draft, Writing - review & editing, Funding acquisition.**Albert Porcar-Castell**:Conceptualization, Formal analysis, Writing - original draft, Writing - review & editing.**Joanna Joiner**:Conceptualization, Formal analysis, Writing - original draft, Writing - review & editing.**Luis Guanter**:Conceptualization, Formal analysis, Writing - original draft, Writing - review & editing.**Xi Yang**:Conceptualization, Formal analysis, Writing - original draft, Writing - review & editing.**Mirco Migliavacca**:Conceptualization, Formal analysis, Writing - original draft, Writing - review & editing.**Weimin Ju**:Formal analysis, Writing - original draft.**Zhigang Sun**:Resources, Writing - original draft.**Shiping Chen**:Resources, Writing - original draft.**David Martini**:Resources, Writing - original draft.**Qian Zhang**:Resources, Writing - original draft.**Zhaohui Li**:Resources, Writing - original draft.**James Cleverly**:Resources, Writing - original draft.**Hezhou Wang**:Resources, Writing - original draft.**Yves Goulas**:Resources.

Declaration of competing interest

The authors declare that they have no known competing financial interests or personal relationships that could have appeared to influence the work reported in this paper.

Acknowledgment

This research was financially supported by the National Key Research and Development Program of China (2019YFA0606601), International Cooperation and Exchange Programme between NSFC and DFG (41761134082), General Program of National Science Foundation of China (41671421), and Academy of Finland (288039). MM and DM received funding from the European Union's Horizon 2020 research and innovation programme under the Marie Sklodowska-Curie grant agreement no. 721995 (TRuStEE). MM and DM thank the Alexander von Humboldt foundation for supporting the research activity in Majadas de Tietar through the Max Planck Research Prize to Markus Reichstein. JJ was supported by NASA through the **Making Earth** System Data Records for Use in Research Environments (**MEaSUREs**) Program. This research was also supported by the Innovative and Practical Program of Graduate Student in Jiangsu Province (SJKY190037).

The authors would thank NASA and the OCO-2 team for making the SIF dataset available. This work used eddy covariance data acquired and shared by the FLUXNET community, including these networks: AmeriFlux, AfriFlux, AsiaFlux, CarboAfrica, CarboEuropeIP, CarboItaly, CarboMont, ChinaFlux, Fluxnet-Canada, GreenGrass, ICOS, KoFlux, LBA, NECC, OzFlux-TERN, TCOS-Siberia, and USCCC. The ERA-Interim reanalysis data are provided by ECMWF and processed by LSCE. The FLUXNET eddy covariance data processing and harmonization was carried out by the European Fluxes Database Cluster, AmeriFlux Management Project, and Fluxdata project of FLUXNET, with the support of CDIAC and ICOS Ecosystem Thematic Center, and the OzFlux, ChinaFlux and AsiaFlux offices. The USDA-ARS supported Cook Agronomy Farm Long-Term Agro-ecosystem Research site provided data for this work. Support for the Reynolds Creek Critical Zone Observatory Cooperative is provided by USDA ARS and NSF Grant #EAR 1331872. OCO-2 SIF product (V8r) is available at https://disc.gsfc.nasa.gov/. TRENDY S3 GPP data from Dr. S. Sitch (s.a.sitch@exeter.ac.uk) upon request. FLUXCOM GPP is available from Dr. Martin Jung (mjung@bgc-jena.mpg.de). VPM GPP is available at https://doi.org/10.6084/m9.figshare.c.3789814. The global C_3/C_4 map was obtained from Dr. Martin Jung (mjung@bgc-jena.mpg.de) upon request. MCD12C1, MCD15A2H, and MCD43A1 are available at https://search.earthdata.nasa.gov/. We greatly appreciate the anonymous reviewers for their insightful and constructive comments that helped us to improve our manuscript.

Appendix A

Table A1
Basic information about field sites for ground continuous SIF and GPP measurements. CRO = crop, GRA = grass, SAV = savanna.

Site ID	Name	Latitude (°)	Longitude (°)	IGBP	Reference
CN-Jrn	Jurong	31.8068	119.2172	CRO (C3: rice)	This study
CN-Shq	Shangqiu	34.5203	115.5894	CRO (C4: corn)	Li et al. (2020)
ES-LM1	Majadas de Tietar - North	39.9427	−5.7786	SAV (EC and SIF measurements conducted on the GRA layer)	El-Madany et al. (2018)
FR-Avg	Avignon	43.9176	4.8796	CRO (C3: wheat)	Daumard et al. (2010)
US-Ha1	Harvard	42.538	−72.171	Forest	Yang et al. (2015)

Table A2
Basic information about flux sites using for OCO-2 SIF-based GPP estimates. ENF = evergreen needleleaf forest, SAV = savanna, GRA = grassland, OSH = open shrubland, EBF = evergreen broadleaf forest, CRO = crop, DBF = deciduous broadleaf forest, CSH = close shrubland, WSA = woody savanna, and MF = mixed forest. C3 and C4 represent C_3 and C_4 plants, respectively.

Site ID	Year	Latitude (°)	Longitude (°)	IGBP	Reference
AU-ASM	2014–2018	−22.2828	133.2493	ENF	Cleverly et al. (2013)
AU-DaS	2014–2018	−14.1592	131.3881	SAV	Beringer et al. (2016)
AU-Dry	2014–2018	−15.2588	132.3706	SAV	Beringer et al. (2016)
AU-GWW	2014–2018	−30.1913	120.6541	SAV	Macfarlane (2013)
AU-Lit	2015–2018	−13.1790	130.7945	SAV	Beringer et al. (2016)
AU-Stp	2014–2018	−17.1507	133.3502	GRA	Beringer et al. (2016)
AU-TTE	2014–2018	−22.2870	133.6400	OSH	Cleverly et al. (2016)
AU-TUM	2014–2018	−35.6566	148.1517	EBF	Woodgate (2013)
AU-Ync	2014–2018	−34.9893	146.2907	GRA	Beringer (2013)
BE-Lon	2014–2017	50.5516	4.7462	CRO (C3: wheat)	Moureaux et al. (2006)
CA-SCC	2015–2016	61.3079	−121.2992	ENF	Helbig et al. (2017)
CN-Dul	2014–2016	42.0467	116.2836	GRA	Chen et al. (2009)
CN-Xil	2014–2018	43.5506	116.6722	GRA	Chen et al. (2009)
CN-Yuc	2015–2017	36.8333	116.5667	CRO (C3: wheat; C4: corn)	Li et al. (2006)
FI-Hyy	2014–2018	61.8474	24.2948	ENF	Suni et al. (2003)
FI-Var	2015–2018	67.7549	29.61	ENF	Ruuskanen et al. (2003)
RU-Fyo	2014–2018	56.4615	32.9221	ENF	Kurbatova et al. (2008)
US-ARM	2014–2018	36.6058	−97.4888	CRO	–
US-Bar	2014–2017	44.0646	−71.2881	DBF	–
US-CF1	2017–2018	46.7815	−117.0821	CRO	–
US-CF2	2017–2018	46.784	−117.0908	CRO	–
US-CF3	2017–2018	46.7551	−117.1261	CRO	–
US-CF4	2017–2018	46.7518	−117.1285	CRO	–
US-GLE	2014–2018	41.3665	−106.2399	ENF	Frank et al. (2014)
US-Ha1	2014–2018	42.5378	−72.1715	DBF	Urbanski et al. (2007)

(*continued on next page*)

Table A2 (*continued*)

Site ID	Year	Latitude (°)	Longitude (°)	IGBP	Reference
US-Ho1	2014–2018	45.2041	−68.7402	ENF	–
US-HRC	2014–2018	34.5857	−91.7475	CRO	–
US-IB1	2014–2017	41.8593	−88.2227	CRO	–
US-RC2	2014–2018	46.7776	−117.0807	CRO	–
US-Rls	2015–2018	43.1439	−116.7356	CSH	–
US-Ro1	2014–2016	44.7143	−93.0898	CRO	Baker and Griffis (2005)
US-Ro2	2015–2016	44.7288	−93.0888	CRO	–
US-Ro5	2017–2018	44.691	−93.0576	CRO	–
US-Ro6	2017–2018	44.6946	−93.0578	CRO	–
US-SRM	2014–2018	31.8214	−110.8661	WSA	Scott et al. (2009)
US-Syv	2014–2018	46.242	−89.3477	MF	Desai et al. (2005)

Appendix B. Supplementary data

Supplementary data to this article can be found online at https://doi.org/10.1016/j.rse.2020.111722.

References

Anav, A., Friedlingstein, P., Beer, C., Ciais, P., Harper, A., Jones, C., et al., 2015. Spatiotemporal patterns of terrestrial gross primary production: a review. Rev. Geophys. 53, 785–818.

Arneth, A., Harrison, S.P., Zaehle, S., Tsigaridis, K., Menon, S., Bartlein, P.J., et al., 2010. Terrestrial biogeochemical feedbacks in the climate system. Nat. Geosci. 3, 525–532.

Badgley, G., Field, C.B., Berry, J.A., 2017. Canopy near-infrared reflectance and terrestrial photosynthesis. Sci. Adv. 3, e1602244.

Baker, J., Griffis, T., 2005. Examining strategies to improve the carbon balance of corn/soybean agriculture using eddy covariance and mass balance techniques. Agric. For. Meteorol. 128, 163–177.

Beadle, C.L., Long, S.P., 1985. Photosynthesis — is it limiting to biomass production? Biomass 8, 119–168.

Beer, C., Reichstein, M., Tomelleri, E., Ciais, P., Jung, M., Carvalhais, N., et al., 2010. Terrestrial gross carbon dioxide uptake: global distribution and covariation with climate. Science 329, 834–838.

Beringer, J., 2013. Yanco JAXA OzFlux Tower Site OzFlux: Australian and New Zealand Flux Research and Monitoring Hdl: 102.100.100/14235.

Beringer, J., Hutley, L.B., McHugh, I., Arndt, S.K., Campbell, D., Cleugh, H.A., et al., 2016. An introduction to the Australian and New Zealand flux tower network – OzFlux. Biogeosciences 13, 5895–5916.

Campbell, J.E., Berry, J.A., Seibt, U., Smith, S.J., Montzka, S.A., Launois, T., et al., 2017. Large historical growth in global terrestrial gross primary production. Nature 544, 84.

Chen, J.M., Leblanc, S.G., 2001. Multiple-scattering scheme useful for geometric optical modeling. IEEE Trans. Geosci. Remote Sens. 39, 1061–1071.

Chen, J., Liu, J., Cihlar, J., Goulden, M., 1999. Daily canopy photosynthesis model through temporal and spatial scaling for remote sensing applications. Ecol. Model. 124, 99–119.

Chen, J.M., Menges, C.H., Leblanc, S.G., 2005. Global mapping of foliage clumping index using multi-angular satellite data. Remote Sens. Environ. 97, 447–457.

Chen, S., Chen, J., Lin, G., Zhang, W., Miao, H., Wei, L., et al., 2009. Energy balance and partition in Inner Mongolia steppe ecosystems with different land use types. Agric. For. Meteorol. 149, 1800–1809.

Cleverly, J., Boulain, N., Villalobos-Vega, R., Grant, N., Faux, R., Wood, C., et al., 2013. Dynamics of component carbon fluxes in a semi-arid Acacia woodland, central Australia. Journal of Geophysical Research: Biogeosciences 118, 1168–1185.

Cleverly, J., Eamus, D., Van Gorsel, E., Chen, C., Rumman, R., Luo, Q., et al., 2016. Productivity and evapotranspiration of two contrasting semiarid ecosystems following the 2011 global carbon land sink anomaly. Agric. For. Meteorol. 220, 151–159.

Collatz, G.J., Ribascarbo, M., Berry, J.A., 1992. Coupled photosynthesis-stomatal conductance model for leaves of C_4 plants. Funct. Plant Biol. 19, 519–538.

Damm, A., Guanter, L., Paul-Limoges, E., van der Tol, C., Hueni, A., Buchmann, N., et al., 2015. Far-red sun-induced chlorophyll fluorescence shows ecosystem-specific relationships to gross primary production: an assessment based on observational and modeling approaches. Remote Sens. Environ. 166, 91–105.

Daumard, F., Champagne, S., Fournier, A., Goulas, Y., Ounis, A., Hanocq, J.F., Moya, I., 2010. A field platform for continuous measurement of canopy fluorescence. IEEE Transactions on Geoscience & Remote Sensing 48, 3358–3368.

Desai, A.R., Bolstad, P.V., Cook, B.D., Davis, K.J., Carey, E.V., 2005. Comparing net ecosystem exchange of carbon dioxide between an old-growth and mature forest in the upper Midwest, USA. Agric. For. Meteorol. 128, 33–55.

Drusch, M., Moreno, J., Del Bello, U., Franco, R., Goulas, Y., Huth, A., et al., 2017. The fluorescence explorer mission concept—ESA's earth explorer 8. IEEE Trans. Geosci. Remote Sens. 55, 1273–1284.

Ehleringer, J., Björkman, O., 1977. Quantum yields for CO_2 uptake in C_3 and C_4 plants: dependence on temperature, CO_2, and O_2 concentration. Plant Physiol. 59, 86–90.

El-Madany, T.S., Reichstein, M., Perez-Priego, O., Carrara, A., Moreno, G., Pilar Martín, M., et al., 2018. Drivers of spatio-temporal variability of carbon dioxide and energy fluxes in a Mediterranean savanna ecosystem. Agric. For. Meteorol. 262, 258–278.

Frank, J.M., Massman, W.J., Ewers, B.E., Huckaby, L.S., Negrón, J.F., 2014. Ecosystem CO_2/H_2O fluxes are explained by hydraulically limited gas exchange during tree mortality from spruce bark beetles. Journal of Geophysical Research: Biogeosciences 119, 1195–1215.

Frankenberg, C., Fisher, J.B., Worden, J., Badgley, G., Saatchi, S.S., Lee, J.E., et al., 2011. New global observations of the terrestrial carbon cycle from GOSAT: patterns of plant fluorescence with gross primary productivity. Geophys. Res. Lett. 38, 351–365.

Frankenberg, C., O'Dell, C., Berry, J., Guanter, L., Joiner, J., Koehler, P., et al., 2014. Prospects for chlorophyll fluorescence remote sensing from the orbiting carbon Observatory-2. Remote Sens. Environ. 147, 1–12.

Friedl, M.A., Sullamenashe, D., Tan, B., Schneider, A., Ramankutty, N., Sibley, A., Huang, X.M., 2010. MODIS collection 5 global land cover: algorithm refinements and characterization of new datasets. Remote Sens. Environ. 114, 168–182.

Friedlingstein, P., Cox, P., Betts, R., Bopp, L., von Bloh, W., Brovkin, V., et al., 2006. Climate–carbon cycle feedback analysis: results from the C^4MIP model intercomparison. J. Clim. 19, 3337–3353.

Friedlingstein, P., Meinshausen, M., Arora, V.K., Jones, C.D., Anav, A., Liddicoat, S.K., Knutti, R., 2014. Uncertainties in CMIP5 climate projections due to carbon cycle feedbacks. J. Clim. 27, 511–526.

Fu, Z., Stoy, P.C., Poulter, B., Gerken, T., Zhang, Z., Wakbulcho, G., Niu, S., 2019. Maximum carbon uptake rate dominates the interannual variability of global net ecosystem exchange. Glob. Chang. Biol. 0.

Gamon, J.A., Somers, B., Malenovský, Z., Middleton, E.M., Rascher, U., Schaepman, M.E., 2019. Assessing vegetation function with imaging spectroscopy. Surv. Geophys. 40, 489–513.

Genty, B., Briantais, J.M., Baker, N.R., 1989. The relationship between the quantum yield of photosynthetic electron transport and quenching of chlorophyll fluorescence. BBA - General Subjects 990, 87–92.

Ghannoum, O., 2008. C_4 photosynthesis and water stress. Ann. Bot. 103, 635–644.

Gitelson, A.A., Buschmann, C., Lichtenthaler, H.K., 1998. Leaf chlorophyll fluorescence corrected for re-absorption by means of absorption and reflectance measurements. J. Plant Physiol. 152, 283–296.

Gitelson, A.A., Viña, A., Ciganda, V., Rundquist, D.C., Arkebauer, T.J., 2005. Remote estimation of canopy chlorophyll content in crops. Geophys. Res. Lett. 32, L08403.

Gitelson, A.A., Arkebauer, T.J., Suyker, A.E., 2018. Convergence of daily light use efficiency in irrigated and rainfed C_3 and C_4 crops. Remote Sens. Environ. 217, 30–37.

Gitelson, A., Viña, A., Solovchenko, A., Arkebauer, T., Inoue, Y., 2019. Derivation of canopy light absorption coefficient from reflectance spectra. Remote Sens. Environ. 231, 111276.

Goulas, Y., Fournier, A., Daumard, F., Champagne, S., Ounis, A., Marloie, O., Moya, I., 2017. Gross primary production of a wheat canopy relates stronger to far red than to red solar-induced chlorophyll fluorescence. Remote Sens. 9, 97.

Gu, L., Han, J., Wood, J.D., Chang, C.Y.-Y., Sun, Y., 2019. Sun-induced Chl fluorescence and its importance for biophysical modeling of photosynthesis based on light reactions. New Phytol. 223, 1179–1191.

Guanter, L., Frankenberg, C., Dudhia, A., Lewis, P.E., Gómez-Dans, J., Kuze, A., et al., 2012. Retrieval and global assessment of terrestrial chlorophyll fluorescence from GOSAT space measurements. Remote Sens. Environ. 121, 236–251.

Guanter, L., Zhang, Y., Jung, M., Joiner, J., Voigt, M., Berry, J.A., et al., 2014. Global and time-resolved monitoring of crop photosynthesis with chlorophyll fluorescence. Proc. Natl. Acad. Sci. U. S. A. 111, E1327–E1333.

Gueymard, C.A., 2001. Parameterized transmittance model for direct beam and circumsolar spectral irradiance. Sol. Energy 71, 325–346.

Haboudane, D., Miller, J.R., Pattey, E., Zarco-Tejada, P.J., Strachan, I.B., 2004. Hyperspectral vegetation indices and novel algorithms for predicting green LAI of crop canopies: modeling and validation in the context of precision agriculture. Remote Sens. Environ. 90, 337–352.

He, L., Chen, J.M., Pisek, J., Schaaf, C.B., Strahler, A.H., 2012. Global clumping index map derived from the MODIS BRDF product. Remote Sens. Environ. 119, 118–130.

He, L., Chen, J.M., Liu, J., Mo, G., Joiner, J., 2017. Angular normalization of GOME-2 sun-induced chlorophyll fluorescence observation as a better proxy of vegetation productivity. Geophys. Res. Lett. 44, 5691–5699.
Helbig, M., Chasmer, L.E., Desai, A.R., Kljun, N., Quinton, W.L., Sonnentag, O., 2017. Direct and indirect climate change effects on carbon dioxide fluxes in a thawing boreal forest-wetland landscape. Glob. Chang. Biol. 23, 3231–3248.
Hovi, A., Raitio, P., Rautiainen, M., 2017. A spectral analysis of 25 boreal tree species. Silva Fenn 51, 1–16.
Joiner, J., Guanter, L., Lindstrot, R., Voigt, M., Vasilkov, A.P., Middleton, E.M., et al., 2013. Global monitoring of terrestrial chlorophyll fluorescence from moderate-spectral-resolution near-infrared satellite measurements: methodology, simulations, and application to GOME-2. Atmospheric Measurement Techniques 6, 2803–2823.
Joiner, J., Yoshida, Y., Zhang, Y., Duveiller, G., Jung, M., Lyapustin, A., et al., 2018. Estimation of terrestrial global gross primary production (GPP) with satellite data-driven models and eddy covariance flux data. Remote Sens. 10, 1346.
Jung, M., Reichstein, M., Margolis, H.A., Cescatti, A., Richardson, A.D., Arain, M.A., et al., 2011. Global patterns of land-atmosphere fluxes of carbon dioxide, latent heat, and sensible heat derived from eddy covariance, satellite, and meteorological observations. J. Geophys. Res. 116, G00J07.
Kellogg, E.A., 2013. C4 photosynthesis. Curr. Biol. 23, R594–R599.
Knyazikhin, Y., Martonchik, J.V., Myneni, R.B., Diner, D.J., Running, S.W., 1998. Synergistic algorithm for estimating vegetation canopy leaf area index and fraction of absorbed photosynthetically active radiation from MODIS and MISR data. Journal of Geophysical Research: Atmospheres 103, 32257–32275.
Knyazikhin, Y., Schull, M.A., Stenberg, P., Mottus, M., Rautiainen, M., Yang, Y., et al., 2013. Hyperspectral remote sensing of foliar nitrogen content. Proc. Natl. Acad. Sci. U. S. A. 110, E185–E192.
Koffi, E.N., Rayner, P.J., Norton, A.J., Frankenberg, C., Scholze, M., 2015. Investigating the usefulness of satellite derived fluorescence data in inferring gross primary productivity within the carbon cycle data assimilation system. Biogeosciences 12, 4067–4084.
Köhler, P., Frankenberg, C., Magney, T.S., Guanter, L., Joiner, J., Landgraf, J., 2018. Global retrievals of solar-induced chlorophyll fluorescence with TROPOMI: first results and intersensor comparison to OCO-2. Geophys. Res. Lett. 45, 10456–10463.
Krall, J.P., Edwards, G.E., 1992. Relationship between photosystem II activity and CO_2 fixation in leaves. Physiol. Plant. 86, 180–187.
Krause, G., Weis, E., 1991. Chlorophyll fluorescence and photosynthesis: the basics. Annu. Rev. Plant Biol. 42, 313–349.
Kulmala, M., Suni, T., Lehtinen, K., Maso, M.D., Boy, M., Reissell, A., et al., 2004. A new feedback mechanism linking forests, aerosols, and climate. Atmos. Chem. Phys. 4, 557–562.
Kulmala, M., Nieminen, T., Nikandrova, A., Lehtipalo, K., Manninen, H.E., Kajos, M.K., et al., 2014. CO_2-induced terrestrial climate feedback mechanism: from carbon sink to aerosol source and back. Boreal Environ. Res. 19, 122–131.
Kurbatova, J., Li, C., Varlagin, A., Xiao, X., Vygodskaya, N., 2008. Modeling carbon dynamics in two adjacent spruce forests with different soil conditions in Russia. Biogeosciences 5, 969–980.
Lee, J.E., Berry, J.A., van der Tol, C., Yang, X., Guanter, L., Damm, A., et al., 2015. Simulations of chlorophyll fluorescence incorporated into the Community Land Model version 4. Glob. Chang. Biol. 21, 3469–3477.
Li, X., Xiao, J.F., 2019. Mapping photosynthesis solely from solar-induced chlorophyll fluorescence: a global, fine-resolution dataset of gross primary production derived from OCO-2. Remote Sens. 11, 2563.
Li, J., Yu, Q., Sun, X., Tong, X., Ren, C., Wang, J., et al., 2006. Carbon dioxide exchange and the mechanism of environmental control in a farmland ecosystem in North China Plain. Sci. China Ser. D Earth Sci. 49, 226–240.
Li, X., Xiao, J., He, B., 2018a. Chlorophyll fluorescence observed by OCO-2 is strongly related to gross primary productivity estimated from flux towers in temperate forests. Remote Sens. Environ. 204, 659–671.
Li, X., Xiao, J., He, B., Arain, M.A., Beringer, J., Desai, A.R., et al., 2018b. Solar-induced chlorophyll fluorescence is strongly correlated with terrestrial photosynthesis for a wide variety of biomes: first global analysis based on OCO-2 and flux tower observations. Glob. Chang. Biol. 24, 3990–4008.
Li, Z., Zhang, Q., Li, J., Yang, X., Wu, Y., Zhang, Z., et al., 2020. Solar-induced chlorophyll fluorescence and its link to canopy photosynthesis in maize from continuous ground measurements. Remote Sens. Environ. 236, 111420.
Liu, J., Chen, J., Cihlar, J., Park, W., 1997. A process-based boreal ecosystem productivity simulator using remote sensing inputs. Remote Sens. Environ. 62, 158–175.
Liu, X., Guanter, L., Liu, L., Damm, A., Malenovský, Z., Rascher, U., et al., 2018. Downscaling of solar-induced chlorophyll fluorescence from canopy level to photosystem level using a random forest model. Remote Sens. Environ. 231, 110772.
Lu, X., Cheng, X., Li, X., Tang, J., 2018. Opportunities and challenges of applications of satellite-derived sun-induced fluorescence at relatively high spatial resolution. Sci. Total Environ. 619–620, 649–653.
MacBean, N., Maignan, F., Bacour, C., Lewis, P., Peylin, P., Guanter, L., et al., 2018. Strong constraint on modelled global carbon uptake using solar-induced chlorophyll fluorescence data. Sci. Rep. 8, 1973.
Macfarlane, C., 2013. Great Western Woodlands OzFlux: Australian and New Zealand Flux Research and Monitoring Hdl: 102.100.100/14229.
Meroni, M., Rossini, M., Guanter, L., Alonso, L., Rascher, U., Colombo, R., Moreno, J., 2009. Remote sensing of solar-induced chlorophyll fluorescence: review of methods and applications. Remote Sens. Environ. 113, 2037–2051.
Miao, G., Guan, K., Yang, X., Bernacchi, C.J., Berry, J.A., DeLucia, E.H., et al., 2018. Sun-induced chlorophyll fluorescence, photosynthesis, and light use efficiency of a soybean field from seasonally continuous measurements. Journal of Geophysical Research: Biogeosciences 123.
Migliavacca, M., Perez-Priego, O., Rossini, M., El-Madany, T.S., Moreno, G., van der Tol, C., et al., 2017. Plant functional traits and canopy structure control the relationship between photosynthetic CO_2 uptake and far-red sun-induced fluorescence in a Mediterranean grassland under different nutrient availability. New Phytol. 214, 1078–1091.
Mohammed, G.H., Colombo, R., Middleton, E.M., Rascher, U., van der Tol, C., Nedbal, L., et al., 2019. Remote sensing of solar-induced chlorophyll fluorescence (SIF) in vegetation: 50 years of progress. Remote Sens. Environ. 231, 111177.
Monteith, J.L., 1972. Solar radiation and productivity in tropical ecosystems. J. Appl. Ecol. 9, 747–766.
Moureaux, C., Debacq, A., Bodson, B., Heinesch, B., Aubinet, M., 2006. Annual net ecosystem carbon exchange by a sugar beet crop. Agric. For. Meteorol. 139, 25–39.
Myneni, R., Knyazikhin, Y., Park, T., 2015. MCD15A2H MODIS/Terra+ Aqua Leaf Area Index/FPAR 8-day L4 Global 500 m SIN Grid V006. (Distributed by NASA EOSDIS Land Processes DAAC).
Mystakidis, S., Davin, E.L., Gruber, N., Seneviratne, S.I., 2016. Constraining future terrestrial carbon cycle projections using observation-based water and carbon flux estimates. Glob. Chang. Biol. 22, 2198–2215.
Norton, A.J., Rayner, P.J., Koffi, E.N., Scholze, M., 2018. Assimilating solar-induced chlorophyll fluorescence into the terrestrial biosphere model BETHY-SCOPE v1. 0: model description and information content. Geosci. Model Dev. 11, 1517–1536.
Pagán, B., Maes, W., Gentine, P., Martens, B., Miralles, D., 2019. Exploring the potential of satellite solar-induced fluorescence to constrain global transpiration estimates. Remote Sens. 11, 413.
Pearcy, R., Ehleringer, J., 1984. Comparative ecophysiology of C_3 and C_4 plants. Plant Cell Environ. 7, 1–13.
Porcar-Castell, A., Tyystjarvi, E., Atherton, J., van der Tol, C., Flexas, J., Pfundel, E.E., et al., 2014. Linking chlorophyll a fluorescence to photosynthesis for remote sensing applications: mechanisms and challenges. J. Exp. Bot. 65, 4065–4095.
Ramos, M.E., Lagorio, M.G., 2006. A model considering light reabsorption processes to correct in vivo chlorophyll fluorescence spectra in apples. Photochemical & Photobiological Sciences 5, 508–512.
Rascher, U., Alonso, L., Burkart, A., Cilia, C., Cogliati, S., Colombo, R., et al., 2015. Sun-induced fluorescence - a new probe of photosynthesis: first maps from the imaging spectrometer HyPlant. Glob. Chang. Biol. 21, 4673–4684.
Reichstein, M., Falge, E., Baldocchi, D., Papale, D., Aubinet, M., Berbigier, P., et al., 2005. On the separation of net ecosystem exchange into assimilation and ecosystem respiration: review and improved algorithm. Glob. Chang. Biol. 11, 1424–1439.
Romero, J.M., Cordon, G.B., Lagorio, M.G., 2018. Modeling re-absorption of fluorescence from the leaf to the canopy level. Remote Sens. Environ. 204, 138–146.
Ruuskanen, T.M., Reissell, A., Keronen, P., Aalto, P.P., Laakso, L., Gronholm, T., et al., 2003. Atmospheric trace gas and aerosol particle concentration measurements in Eastern Lapland, Finland 1992–2001. Boreal Environ. Res. 8, 335–350.
Sage, R.F., Kubien, D.S., 2007. The temperature response of C_3 and C_4 photosynthesis. Plant Cell Environ. 30, 1086–1106.
Schaaf, C.B., Gao, F., Strahler, A.H., Lucht, W., Li, X., Tsang, T., et al., 2002. First operational BRDF, albedo nadir reflectance products from MODIS. Remote Sens. Environ. 83, 135–148.
Scott, R.L., Jenerette, G.D., Potts, D.L., Huxman, T.E., 2009. Effects of seasonal drought on net carbon dioxide exchange from a woody-plant-encroached semiarid grassland. Journal of Geophysical Research: Biogeosciences 114, G04004.
Sitch, S., Friedlingstein, P., Gruber, N., Jones, S.D., Murray-Tortarolo, G., Ahlström, A., et al., 2015. Recent trends and drivers of regional sources and sinks of carbon dioxide. Biogeosciences 12, 653–679.
Smith, W.K., Reed, S.C., Cleveland, C.C., Ballantyne, A.P., Anderegg, W.R., Wieder, W.R., et al., 2016. Large divergence of satellite and earth system model estimates of global terrestrial CO_2 fertilization. Nat. Clim. Chang. 6, 306.
Smolander, S., Stenberg, P., 2005. Simple parameterizations of the radiation budget of uniform broadleaved and coniferous canopies. Remote Sens. Environ. 94, 355–363.
Still, C.J., Berry, J.A., Collatz, G.J., DeFries, R.S., 2003. Global distribution of C_3 and C_4 vegetation: carbon cycle implications. Glob. Biogeochem. Cycles 17, 1006.
Sun, Y., Frankenberg, C., Wood, J.D., Schimel, D.S., Jung, M., Guanter, L., et al., 2017. OCO-2 advances photosynthesis observation from space via solar-induced chlorophyll fluorescence. Science 358, eaam5747.
Sun, Y., Frankenberg, C., Jung, M., Joiner, J., Guanter, L., Köhler, P., Magney, T., 2018. Overview of Solar-Induced chlorophyll Fluorescence (SIF) from the Orbiting Carbon Observatory-2: retrieval, cross-mission comparison, and global monitoring for GPP. Remote Sens. Environ. 209, 808–823.
Suni, T., Rinne, J., Reissell, A., Altimir, N., Keronen, P., Rannik, U., et al., 2003. Long-term measurements of surface fluxes above a Scots pine forest in Hyytiala, southern Finland, 1996–2001. Boreal Environ. Res. 8, 287–302.
van der Tol, C., Berry, J.A., Campbell, P.K.E., Rascher, U., 2014. Models of fluorescence and photosynthesis for interpreting measurements of solar-induced chlorophyll fluorescence. Journal of Geophysical Research: Biogeosciences 119, 2312–2327.
Tramontana, G., Jung, M., Schwalm, C.R., Ichii, K., Camps-Valls, G., Raduly, B., et al., 2016. Predicting carbon dioxide and energy fluxes across global FLUXNET sites with regression algorithms. Biogeosciences 13, 4291–4313.
Urbanski, S., Barford, C., Wofsy, S., Kucharik, C., Pyle, E., Budney, J., et al., 2007. Factors controlling CO_2 exchange on timescales from hourly to decadal at Harvard Forest. Journal of Geophysical Research: Biogeosciences 112, G02020.
Verma, M., Schimel, D., Evans, B., Frankenberg, C., Beringer, J., Drewry, D.T., et al., 2017. Effect of environmental conditions on the relationship between solar-induced fluorescence and gross primary productivity at an OzFlux grassland site. Journal of Geophysical Research: Biogeosciences 122, 716–733.
Wood, J.D., Griffis, T.J., Baker, J.M., Frankenberg, C., Verma, M., Yuen, K., 2017. Multiscale analyses of solar-induced florescence and gross primary production.

Geophys. Res. Lett. 44, 533–541.
Woodgate, W., 2013. Tumbarumba OzFlux Tower Site OzFlux: Australian and New Zealand Flux Research and Monitoring hdl: 102.100.100/14241.
Yang, P., van der Tol, C., 2018. Linking canopy scattering of far-red sun-induced chlorophyll fluorescence with reflectance. Remote Sens. Environ. 209, 456–467.
Yang, X., Tang, J., Mustard, J.F., Lee, J.-E., Rossini, M., Joiner, J., et al., 2015. Solar-induced chlorophyll fluorescence that correlates with canopy photosynthesis on diurnal and seasonal scales in a temperate deciduous forest. Geophys. Res. Lett. 42, 2977–2987.
Yang, K., Ryu, Y., Dechant, B., Berry, J.A., Hwang, Y., Jiang, C., et al., 2018a. Sun-induced chlorophyll fluorescence is more strongly related to absorbed light than to photosynthesis at half-hourly resolution in a rice paddy. Remote Sens. Environ. 216, 658–673.
Yang, X., Shi, H., Stovall, A., Guan, K., Miao, G., Zhang, Y., et al., 2018b. FluoSpec 2—an automated field spectroscopy system to monitor canopy solar-induced fluorescence. Sensors 18, 2063.
Zeng, Y., Badgley, G., Dechant, B., Ryu, Y., Chen, M., Berry, J., 2019a. A practical approach for estimating the escape ratio of near-infrared solar-induced chlorophyll fluorescence. Remote Sens. Environ. 232, 211209.
Zeng, Y., Badgley, G., Dechant, B., Ryu, Y., Chen, M., Berry, J., 2019b. A practical approach for estimating the escape ratio of near-infrared solar-induced chlorophyll fluorescence. Remote Sens. Environ. 211209.
Zhang, Y.G., Guanter, L., Berry, J.A., Joiner, J., van der Tol, C., Huete, A., et al., 2014. Estimation of vegetation photosynthetic capacity from space-based measurements of chlorophyll fluorescence for terrestrial biosphere models. Glob. Chang. Biol. 20, 3727–3742.
Zhang, Y.G., Guanter, L., Berry, J.A., van der Tol, C., Yang, X., Tang, J., Zhang, F., 2016. Model-based analysis of the relationship between sun-induced chlorophyll fluorescence and gross primary production for remote sensing applications. Remote Sens. Environ. 187, 145–155.
Zhang, Y., Xiao, X., Wu, X., Zhou, S., Zhang, G., Qin, Y., Dong, J., 2017. A global moderate resolution dataset of gross primary production of vegetation for 2000–2016. Scientific Data 4, 170165.
Zhang, Y., Xiao, X., Zhang, Y., Wolf, S., Zhou, S., Joiner, J., et al., 2018a. On the relationship between sub-daily instantaneous and daily total gross primary production: implications for interpreting satellite-based SIF retrievals. Remote Sens. Environ. 205, 276–289.
Zhang, Y.G., Guanter, L., Joiner, J., Song, L., Guan, K., 2018b. Spatially-explicit monitoring of crop photosynthetic capacity through the use of space-based chlorophyll fluorescence data. Remote Sens. Environ. 210, 362–374.
Zhang, Z.Y., Zhang, Y.G., Joiner, J., Migliavacca, M., 2018c. Angle matters: bidirectional effects impact the slope of relationship between gross primary productivity and sun-induced chlorophyll fluorescence from Orbiting Carbon Observatory-2 across biomes. Glob. Chang. Biol. 24, 5017–5020.
Zhang, Z.Y., Chen, J.M., Guanter, L., He, L.M., Zhang, Y.G., 2019. From canopy-leaving to total canopy far-red fluorescence emission for remote sensing of photosynthesis: first results from TROPOMI. Geophys. Res. Lett. 46, 12030–12040.
Zhu, Z., Piao, S., Myneni, R.B., Huang, M., Zeng, Z., Canadell, J.G., et al., 2016. Greening of the earth and its drivers. Nat. Clim. Chang. 6, 791–795.